Research Square

Preprints are preliminary reports that have not undergone peer review.
They should not be considered conclusive, used to inform clinical practice,
or referenced by the media as validated information.

Mechanical Behavior and Topological Damage Mechanism of Shaped Fragments Penetrating 2A12 Aluminum Alloy Targets under Complex Attitudes

Zhitao Dong
Northeastern University
Bo Hao
2361465215@qq.com
Northeastern University
Kun Duan
Northeastern University
Zixu Chen
Northeastern University

Research Article

Keywords: Dynamic plasticity, Contact topology, Energy dissipation, Ballistic limit, Finite element analysis, Mechanics-based design

Posted Date: November 27th, 2026

DOI: https://doi.org/10.21203/rs.3.rs-11701139/v1

License: This work is licensed under a Creative Commons Attribution 4.0 International License.
Read Full License

Additional Declarations: No competing interests reported.

Mechanical Behavior and Topological Damage Mechanism of Shaped Fragments Penetrating 2A12 Aluminum Alloy Targets under Complex Attitudes

Zhitao Dong[a,b] , Bo Hao[a,b], Kun Duan[a] , and Zixu Chen[a,b]

[a]Key Laboratory of Vibration and Control of Aeronautical Power Equipment of Ministry of Education, Northeastern University at Qinhuangdao, Qinhuangdao, 066000, Hebei, China. [b]School of Mechanical Engineering and Automation, Northeastern University, Shenyang, 110819, China.

[*]e-mail:2361465215@qq.com

Abstract–Thin metallic plates subjected to high-velocity impact exhibit strongly configuration-dependent failure, yet the mechanical link between the impactor's contact topology and the resulting energy-dissipation pathway remains poorly quantified for non-axisymmetric bodies. This work investigates nine equal-volume fragments—differing in cross-sectional eccentricity, aspect ratio and rhombic mesh angle—perforating 5-mm-thick 2A12 aluminium alloy plates, using Abaqus/Explicit simulations with Johnson–Cook plasticity and damage models plus a Mie–Grüneisen equation of state. The model is validated against ballistic tests, with a maximum ballistic-limit deviation of 4.17%. Parametric studies cover impact velocities of 200–800 m/s, plate thicknesses of 1–5 mm and non-ideal attitudes, decoupling the angle of incidence from the angle of attack. A topological damage dimensionality index is proposed to correlate the transient point-, line- or face-contact configuration with stress localization and plastic-work partitioning; it predicts ballistic limits more reliably than static descriptors such as sectional density or aspect ratio. Lowering the contact dimensionality suppresses global plastic bending and promotes localized adiabatic shear and ductile tearing, reducing the ballistic limit by up to 40%. Sharp leading edges generate a chiselling effect that stabilizes the trajectory and postpones ricochet at large incidence angles, whereas flat noses suffer embedment; conversely, slender geometries retain as little as 30% of their normal-attitude residual velocity under transverse attack. These results furnish a mechanics-based criterion for balancing penetration capability against attitude robustness in impactor shape design.

Keywords: Dynamic plasticity; Contact topology; Energy dissipation; Ballistic limit; Finite element analysis; Mechanics-based design

1. INTRODUCTION

In the fields of modern terminal ballistics and high-velocity penetration mechanics, the dynamic impact response of fragments on lightweight armored protective structures has consistently remained a core proposition of solid mechanics research [1–5]. The terminal ballistic performance and penetration efficiency of fragments are largely governed by their geometric topologies. Conventional studies have predominantly focused on the penetration laws of simple geometric bodies, comprehensively exploring failure mechanisms of target plates under various strain rates, such as adiabatic shear, ductile tearing, and cavity expansion [6–10]. However,

in actual damage engineering, shaped fragments frequently exhibit highly complex topological features. These macroscopic geometric parameters define the 'topological damage dimensionality' during the fragment-target interaction. Subsequently, this dimensionality dictates the specific energy dissipation pathways through which the impact kinetic energy is transferred to the target. More importantly, given that fragments are highly prone to attitude deflections during actual dispersal and aerodynamic flight, their target-striking attitudes exhibit significant randomness and instability [11–13].

Within this domain, previous investigations concerning the penetration behavior of aluminum alloy targets can be broadly classified into two categories: the influence of projectile geometric characteristics (e.g., nose shape and caliber) and the effects of complex impact conditions (e.g., target structural configuration and impact attitude).

In past studies regarding projectile geometry, it has been well established that the topological characteristics of the impactor fundamentally dictate the failure mechanisms and energy dissipation pathways of the target. For instance, Gupta et al. [14, 15] and Senthil [16] (utilizing the experimental data of Levy et al. [17]) demonstrated that projectile nose shape—specifically sharp-nosed, blunt, and hemispherical configurations—significantly alters ballistic performance. Their findings indicated that sharp-nosed projectiles exhibit superior penetration efficiency in thin targets. Conversely, blunt projectiles minimize perforation energy consumption in thick targets by inducing localized plugging. This localized failure mode contrasts sharply with the global dishing deformation caused by hemispherical noses. Furthermore, geometrical scale effects, such as projectile caliber [18] and cone angle [19], have been proven to exhibit a distinct linear or monotonic correlation with the ballistic limit. Regarding energy dissipation pathways during penetration, numerous researchers have made outstanding contributions. By investigating the penetration and impact behaviors of blunt [20] and sharp-nosed projectiles [21, 22], Woodward proposed a set of theoretical impact models tailored to specific geometries, clearly elucidating the energy dissipation mechanisms during the penetration process. Concurrently, Ben-Dor et al. employed an equilibrium approach to specifically investigate the internal damage of target plates subjected to projectile penetration, simulating internal friction, shear forces, and inertial effects. Today, with advancements in research methodologies, theoretical quantification of energy dissipation at specific penetration stages can be achieved to varying degrees. For example, Chen and Li [23-27] simulated penetration and shear effects across different stages for projectiles with diverse geometries and features (e.g., deformability). Portions of their work, alongside the studies of the aforementioned researchers, have made significant contributions to the theoretical quantification of adiabatic shear energy dissipation during penetration.

Beyond projectile geometry, the penetration resistance of target plates is highly sensitive to external impact boundary conditions. Previously, Iqbal et al. [19] confirmed that an increase in the incident angle drastically elevates the ultimate penetration velocity of the projectile. Similarly, the structural complexity of target plates (e.g., laminated configurations and moving states) has been shown to result in

the progressive degradation of ballistic resistance under multiple impacts [28]. Moreover, recent studies in this field indicate that characterizing the resistance of finite-thickness targets remains challenging. Existing theoretical models typically rely on piecewise empirical functions, which introduce non-physical resistance discontinuities during the transition from cavity expansion to shear plugging [29]. Additionally, classical penetration theoretical frameworks are predominantly validated on low-strength aluminum alloys, frequently failing to accurately capture real-time energy partitioning and dynamic resistance fluctuations under more complex material or geometric constraints [30].

Despite these valuable insights, a critical assessment of the existing literature reveals that the majority of studies remain confined to the mechanical behaviors of standard axisymmetric projectiles (e.g., spheres or regular cylinders) under idealized orthogonal or simple oblique penetration trajectories. At present, a comprehensive understanding of the penetration mechanisms of asymmetric shaped fragments under highly stochastic three-dimensional flight attitudes remains scarce. Specifically, current research lacks a systematic quantitative analysis concerning the synergistic influences among fragment topological damage dimensionality, target plate thickness, and non-ideal attitude perturbations. In particular, it is imperative to explicitly distinguish and decouple the independent mechanical effects of the incident angle (which alters the effective target thickness) and the angle of attack (which alters the initial contact topology).

To address this research gap, the present study systematically investigates the dynamic penetration behaviors of nine distinct shaped fragments. These fragments impact 5-mm-thick 2A12 aluminum alloy target plates. The entire investigation is conducted utilizing the Abaqus/Explicit numerical simulation framework. This study not only evaluates the penetration mechanical responses of fragments under various impact velocities and target thicknesses, but also emphatically analyzes the independent influences of non-ideal target-striking attitudes—specifically the incident angle and the angle of attack—on the ballistic limit and damage failure modes. This study introduces the governing concept of 'topological damage' dimensionality to elucidate specific mesomechanical mechanisms. Specifically, it demonstrates how 'point-contact' and 'line-contact' configurations effectively suppress global plastic bending. Consequently, this suppression significantly reduces the target's ballistic limit. Concurrently, this study reveals the anti-ricochet "chiseling effect" induced by sharp edges at large incident angles, as well as the severe "target plugging" failure mechanism encountered by flat-nosed configurations. The present research aims to elucidate the trade-off relationship between the ultimate penetration lethality of fragments and their aerodynamic attitude robustness, thereby providing a solid theoretical foundation for the optimized design of high-efficiency lethal fragments.

2. Experimental and Theoretical Framework

2.1 Establishment of the Penetration Model

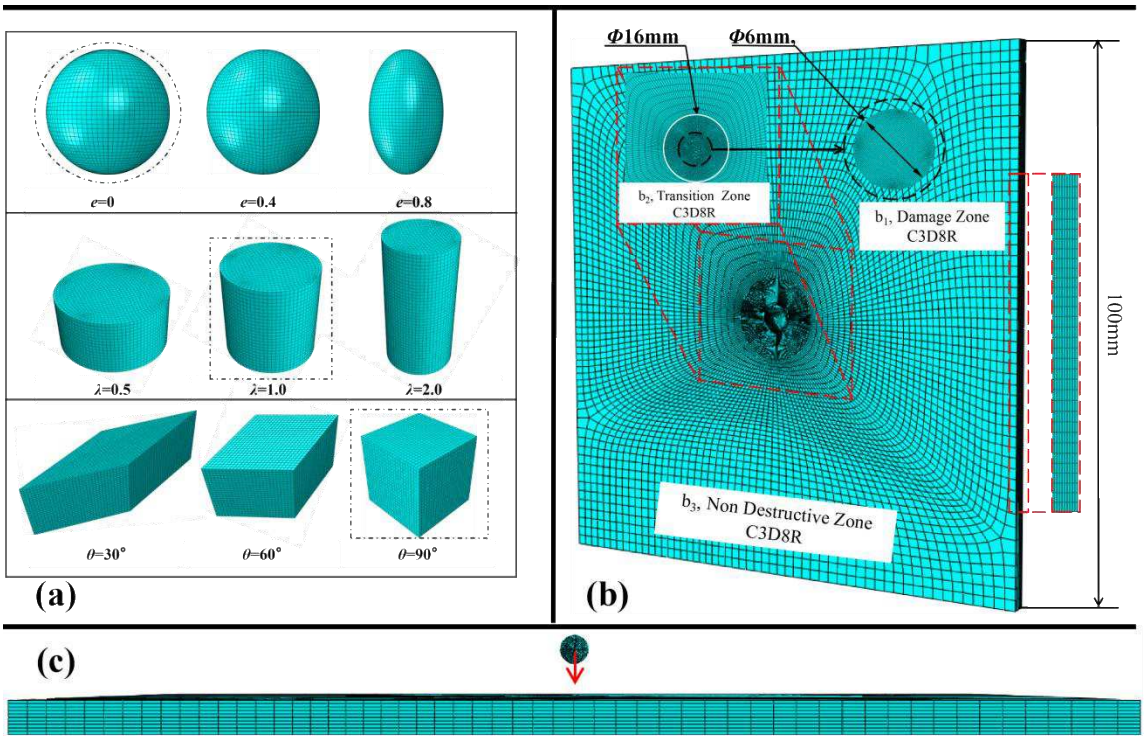


Fig. 1. Schematic of the penetration model.
(a) Fragment meshing model(b) Target plate meshing model, b_1 is the damage zone, b_2 is the transition zone, and b_3 is the non damage zone. The meshing type is C3D8R, and the sizes are 0.1mm, 0.3mm, and 2mm models, respectively(c) Fragment-target assembly diagram

In this study, spherical, cubic, and cylindrical shapes are selected as the baseline geometries, from which nine derivative configurations are extended and constructed. These consist of spheres with three different cross-sectional eccentricities e, cylinders with three different aspect ratios λ, and cubes with three different rhombic angles θ. In total, three series comprising nine fragment structural morphologies encompass point-, line-, and face-contact damage modes, which are sufficient to address most scenarios in a variable three-dimensional space where damage effectiveness is compromised due to fragment morphology.

Among specialized fragment materials such as lead, tungsten alloy, copper, and alloy steel, tungsten alloy provides a greater projectile core mass within an identical volume. Furthermore, millimeter-scale tungsten spheres are capable of maintaining effective lethal kinetic energy over longer distances after being explosively driven [31, 32]. Consequently, tungsten alloy is preferentially selected as the fragment material. All fragments maintain an identical volume of 7 mm^3 to guarantee identical initial kinetic energy at the same impact velocity. The nine fragment morphologies are modeled using the Abaqus/Explicit module, and structured hexahedral meshes are individually partitioned according to the specific geometric shape and dimensional parameters of each fragment. The mesh size for all fragment configurations is meticulously refined to 0.10 mm, and all mesh elements are designated as C3D8R. The finite element mesh models of the nine fragment configurations are illustrated in

Fig. 1(a), wherein the standard baseline geometries are enclosed by the black dashed boxes.

Owing to its excellent properties—such as high strength, low density, corrosion resistance, and cost-effectiveness—2A12 aluminum alloy possesses considerable research value in the field of fragment penetration [33–35]; consequently, it is selected as the target plate material in the present study. To account for the spatial proximity effects relative to the target center, the planar dimensions of the target plate are specified as 100 mm × 100 mm, which is significantly larger than the damage cross-section of the fragment. The global mesh size of the target plate is set to 2.0 mm. To optimize computational resources, the target plate is partitioned into a damage zone, a transition zone, and a non-damage zone corresponding to the penetration process of the fragment. To guarantee simulation fidelity, structured hexahedral meshes composed of C3D8R elements are utilized across all three regions. The cross-sections of the damage and transition zones are geometrically defined as concentric circles centered at the target plate's centroid, with diameters of 6 mm and 16 mm, respectively. Localized mesh refinement is implemented, achieving an element size of 0.1 mm within the damage zone and 0.3 mm within the transition zone. This graded meshing strategy, wherein the element size progressively increases radially outward from the center, adequately captures the propagation characteristics of the shock waves generated during the fragment's penetration into the target. In the thickness direction, the mesh size is uniformly specified as one-tenth of the total target thickness, thereby discretizing the plate into 10 uniform layers. Fig. 1(b) illustrates the meshed finite element model of the target plate, and Fig. 1(c) displays the fragment-target assembly diagram.

2.2 Determination of Material Parameters for the Fragment and Target Plate

The material behaviors of both the tungsten alloy fragment and the target plate are delineated utilizing the Johnson-Cook (JC) constitutive model and the Johnson-Cook damage model. The JC constitutive model features clear physical significance and high computational fidelity, rendering it highly adaptable to the vast majority of high-strain-rate and large-deformation scenarios. Functioning as an ideal rigid-plastic model, it exhibits an exceptional capability to capture the strain-rate and strain-hardening effects of metallic materials [36]. The mathematical formulation of this model is expressed as follows:

$$\sigma_\rho=\left(A+B\varepsilon_\rho^n\right)\left(1+C\ln\dot{\varepsilon}^*\right)\left(1-T^{*m}\right) \tag{2.1}$$

In this model, σ_ρ represents the equivalent stress; A and B denote the yield stress and strain hardening coefficient of the material under reference strain rate and reference temperature conditions, respectively; C is the strain rate sensitivity coefficient; m is the temperature softening exponent; n is the strain hardening exponent; $\varepsilon=\left(\varepsilon_\rho/\varepsilon_0\right)-1$ represents the dimensionless equivalent plastic strain rate; ε and ε_0 are the equivalent plastic strain and reference strain rate, respectively; $T^*=(T-T_\mathrm{r})/(T_\mathrm{m}-T_\mathrm{r})$ is the temperature softening factor, where T_r is the reference

temperature, T_m is the material's melting point, and T is the actual temperature.

In the domain of fragment penetration, the JC damage model is invariably prioritized within finite element frameworks owing to its robust capability to effectively represent the failure behaviors of metallic materials subjected to high strain rates and severe deformations. Its expression is formulated as follows:

$$\varepsilon_f=[D_1+D_2\varepsilon^{D_3\eta}](1+D_4\ln\varepsilon^n)(1-D_5T^m) \tag{2.2}$$

In this model, ε_f represents the fracture strain value under a specific stress, strain rate, and temperature environment; η corresponds to the measure of the stress triaxiality. D_1 to D_5 are the key parameters of the material during the damage-to-failure process.

The JC material model parameters for the tungsten alloy fragments are detailed in Table 1 [37, 38], whereas the corresponding JC material model parameters for the 2A12 aluminum alloy target plate are presented in Table 2 [39].

Table 1. JC material parameters of tungsten alloy fragments

Material	ρ/kg·m^{-3}	E/GPa	m	G/GPa	A/MPa	B/MPa	C	n
Tungsten Alloy	17650	410	1.0	137	1500	177	0.016	0.12
Material	Tm/K	Tr/K	ε^0/s^{-1}	D1	D2	D3	D4	D5
Tungsten Alloy	1498	298	1.0	2.0	1.77	-3.4	0	0

Table 2. JC material parameters of aluminum alloy target plate

Material	ρ/kg·m^{-3}	E/GPa	G/GPa	A/MPa	B/MPa	C	n	m
Aluminum Alloy	2780	73.083	26.9	369	684	0.0083	0.83	1.7
Material	Tm/K	Tr/K	D1	D2	D3	D4	D5	ε^0/s^{-1}
Aluminum Alloy	775	300	0.13	0.13	-0.15	0.011	0.0	5E-4

Furthermore, an Equation of State (EOS) is incorporated into the simulation framework of the present study to characterize the hydrodynamic responses during the interaction of the assembly components. Specifically, during severe material deformation, the Mie-Grüneisen EOS provides the mathematical formulation delineating the relationship between the hydrostatic pressure experienced by the material and other pertinent thermodynamic variables:

$$p_h=\rho_0c_v^2\mu+(\gamma_0+a\mu)E_0 \tag{2.3}$$

where c_v denotes the bulk speed of sound; γ_0 represents the Grüneisen gamma coefficient; a acts as the first-order volume correction coefficient; and E_0 and ρ_0 indicate the initial internal energy per unit volume and the initial mass density of the material, respectively.

When the material is subjected to compressive effects, the Mie-Grüneisen equation of state is conventionally employed to define the hydrostatic pressure sustained by the material. Its specific formulation is expressed as follows:

$$p_h=\frac{\rho_0 c_v^2\mu\left[1+\left(1-\frac{\gamma_0}{2}\right)\mu-\frac{a}{2}\mu^2\right]}{\left[1-(S_1-1)\mu-S_2\frac{\mu^2}{\mu+1}-S_3\frac{\mu^3}{(\mu+1)^2}\right]^2}+(\gamma_0+a\mu)E \tag{2.4}$$

$$\mu=\frac{\rho}{\rho_0}-1 \tag{2.5}$$

where S_1 through S_3 denote the slope coefficients corresponding to distinct segments of the curve, respectively. The equation of state parameters for both the tungsten alloy fragments and the 2A12 aluminum alloy target plate are presented in Table 3 [37, 38].

Table 3. Tungsten alloy and aluminum alloy equation of state parameters

Material	S_1	S_2	S_3	γ^0	a	$Cv/m{\cdot}s^{-1}$	$E_0/J{\cdot}m^{-3}$
Tungsten Alloy	1.237	0.0	0.0	1.54	0.0	40293	0.0
Aluminum Alloy	1.4	0.0	0.0	1.97	0.0	5240	0.0

2.3 Validation of the Numerical Model

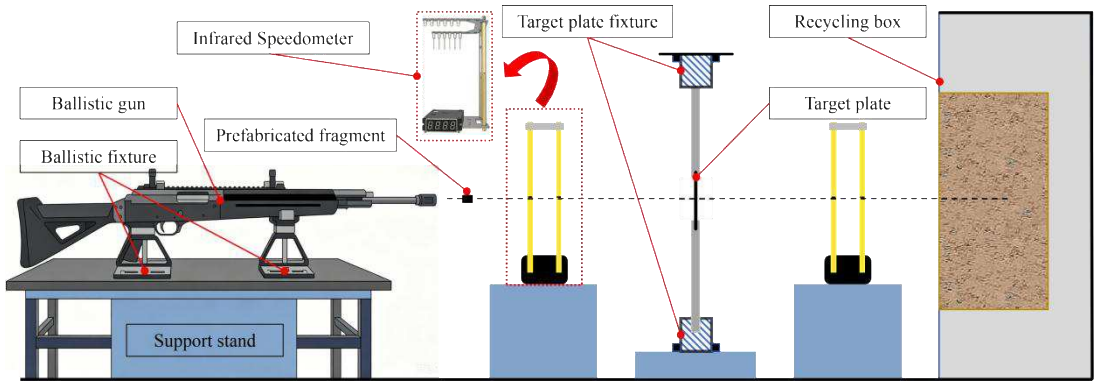


Fig. 2. Schematic diagram of experimental device layout.

Table 4. Comparison between the experimental and simulated ballistic limits of tungsten spheres penetrating 2A12 aluminum plates [40]

Parameter	Number					
	1	2	3	4	5	6
Caliber(mm)	10	7	3	3	3.8	4
Target thickness(mm)	8	8	8	2	2	2
Test value (m/s)	306	423	806	288	243	233
Simulated Value(m/s)	311	430	823	300	251	241
Simulation Error(%)	1.63	1.65	2.11	4.17	3.29	3.43

To validate the effectiveness of the numerical model established in this study, ballistic penetration tests were conducted targeting the baseline geometries of the three fragment series. The schematic diagram of the experimental setup is illustrated in Fig. 2. Concurrently, taking into account the inherent difficulties in precisely controlling the target-striking attitudes of the shaped fragments during physical testing,

the ballistic penetration experiments conducted herein are exclusively intended to verify the feasibility and accuracy of the primary methodology employed in this study, namely the finite element simulation.

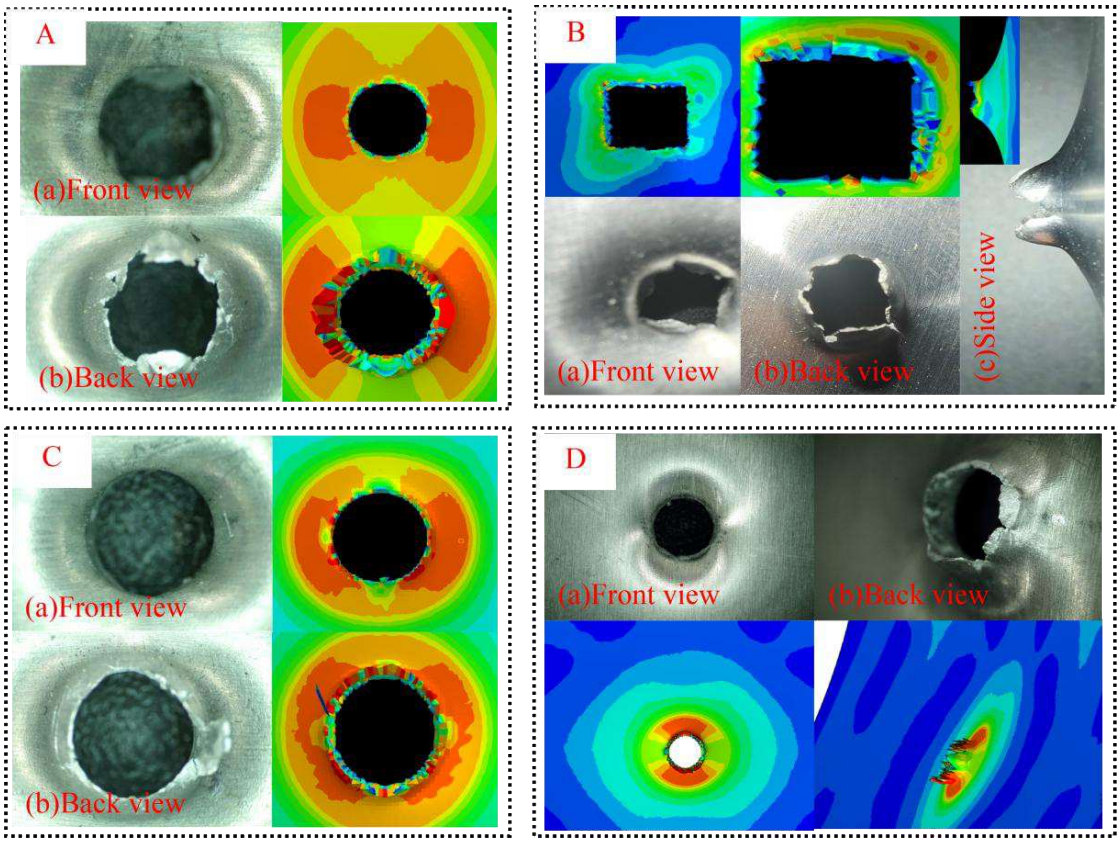


Fig.3. Comparison between simulated and experimentally observed damage modes.

3. NUMERICAL SIMULATION RESULTS AND ANALYSIS

A comparison between the simulated and experimentally observed damage modes is illustrated in Fig. 3. Specifically, A depicts a fragment with a morphology of e=0 (i.e., a sphere) penetrating a 1-mm-thick aluminum target at an impact velocity of 472 m/s; B represents a fragment with θ=90° (i.e., a cube) penetrating a 0.5-mm-thick aluminum target at 183 m/s; C denotes a fragment with λ=1.0 (i.e., a standard cylinder) penetrating a 1-mm-thick aluminum target at 367 m/s; and D illustrates a prior experimental and numerical comparative study conducted by our research group, in which a 3-mm-diameter tungsten alloy sphere impacted a 2A12 aluminum alloy target plate (thickness: 2 mm, curvature: 1/80) at a velocity of 511 m/s. Furthermore, the ballistic limit data derived from experiments conducted on spherical fragments of specific dimensions are presented in Table 4, utilizing a methodology consistent with the present study [40]. The results indicate that the maximum discrepancy between the simulated and experimental values is 4.17%, and the perforation damage morphologies generated by the numerical simulations exhibit a high degree of consistency with the experimental observations. This demonstrates that the numerical model established in the present study possesses sufficient validity.

Utilizing the Abaqus/Explicit dynamic module, the penetration behaviors of nine fragment morphologies across three distinct series are systematically investigated

under various impact velocities, different 2A12 aluminum alloy target plate thicknesses, and diverse target-striking attitudes. Furthermore, the post-penetration deformation of the target plate, the residual velocity of the fragments, the ballistic limits, and the energy consumption during the perforation process are comprehensively analyzed.

3.1 Residual velocity analysis

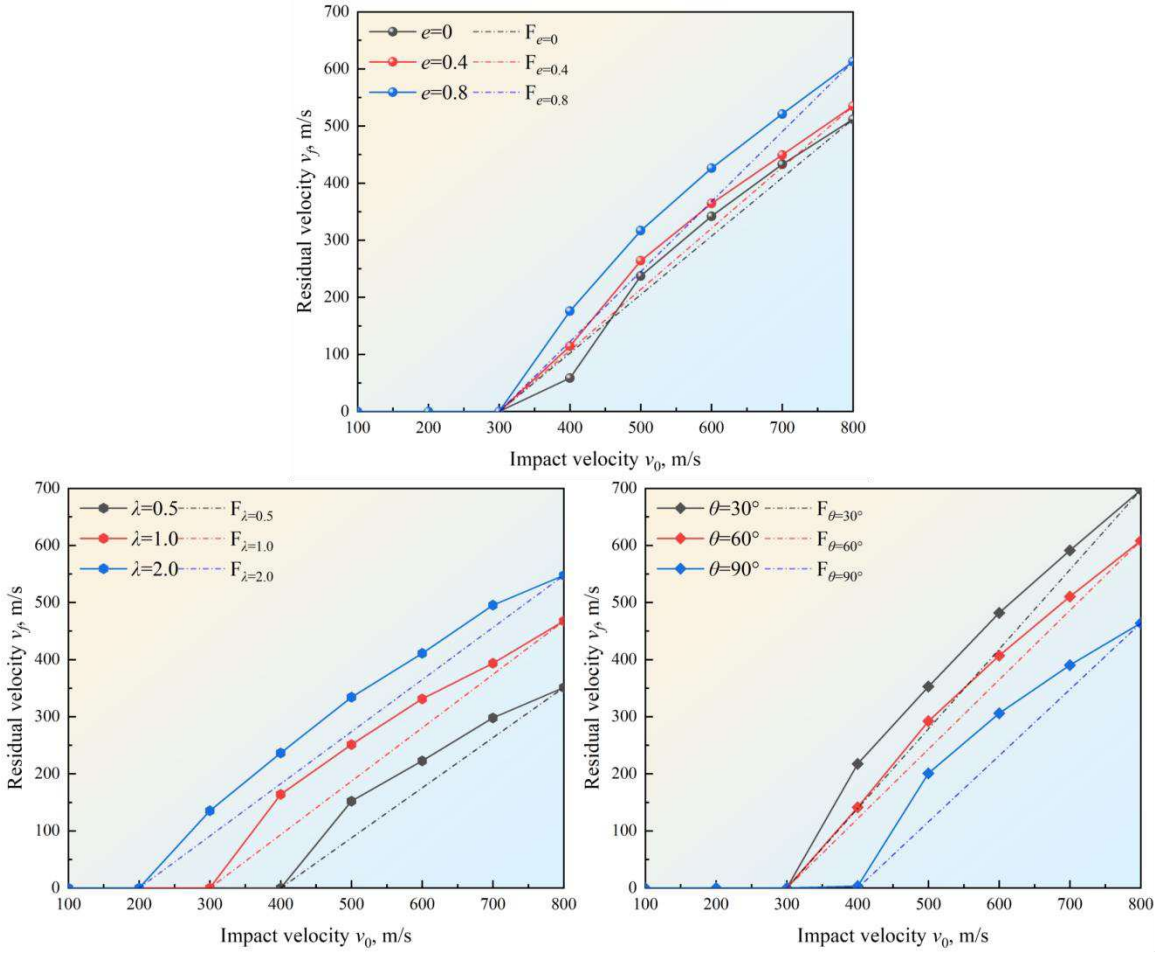


Fig.4. Residual velocity curves of various fragment morphologies penetrating the aluminum alloy target plate under different impact velocities.

Under the condition of normal penetration into a 5-mm-thick target plate, the residual velocity evolution of the nine fragment morphologies at varying impact velocities is illustrated in Fig. 4. As deduced from the numerical trends, at low impact velocities ($v_0 \leq 200$m/s), none of the fragment configurations effectively perforate the target plate, indicating that the ballistic limit velocities for all fragments strictly exceed 200 m/s. Furthermore, with an increment in the initial impact velocity, the residual velocity correspondingly exhibits a monotonically increasing trend. This demonstrates that, for a constant target thickness, once a critical velocity threshold is surpassed, the ballistic resistance exerted by the target plate against the fragment becomes markedly limited.

For the spherical series of fragment morphologies, the residual velocity exhibits a progressive increase with an increment in eccentricity e. This originates from the fact that, when both the incident angle and the angle of attack are exactly 0°, the

penetration behavior of the *e*-series morphologies manifests as a classical "point-contact damage" mode. The core characteristic of point-contact damage is the extreme concentration of energy; upon impact, kinetic energy converges exclusively through a minuscule contact point, generating localized compressive stress waves of ultra-high amplitude at the center of the impact zone on the target plate. As the eccentricity e increases, the radius of curvature at the fragment nose decreases, which further elevates the sharpness of this "point-contact damage." Under these conditions, the mechanical response of the target material highly conforms to the cylindrical or spherical cavity expansion theory. A larger e value necessitates less transverse plastic work to displace the target material, resulting in a lower kinetic energy dissipation rate. Consequently, this macroscopically translates to a substantial elevation in residual velocity and a significant reduction in the ballistic limit.

For the cylindrical series of fragment morphologies, the residual velocity similarly demonstrates a monotonically increasing trend as the aspect ratio λ increases. Under this specific condition, the initial contact surface of the cylindrical fragment constitutes a complete two-dimensional circular area, representing a typical "face-contact damage" mode. Its distinguishing feature is the broad spatial dispersion of energy and its global coupling with the target plate, leading to a drastic decline in the specific kinetic energy per unit area. When the cylinder aspect ratio λ=0.5 (flat cylinder), the "face-contact damage" effect reaches its maximum threshold. As λ increases to 2.0 (slender cylinder), the striking cross-sectional area sharply contracts. Physically, this mechanism fundamentally forces a dimensional reduction from "face-contact damage" to "point-contact damage." The reduction in the contact surface effectively suppresses the global plastic bending of the target plate, transforming the penetration mode into highly efficient localized shear plugging, thereby realizing a surge in residual velocity and a precipitous drop in the ballistic limit.

Conversely, for the rhombic cylinder fragment morphologies, the residual velocity demonstrates a descending trend as the rhombic mesh angle θ increases. The rhombic cylinder fragment impacts the target plate via its lateral edge or wedge-shaped blade, rendering the initial contact surface a spatial line segment and thereby inducing a "line-contact damage" mode. Compared to the radial extrusion characteristic of "point-contact damage," line contact generates extremely high shear and tensile stress concentrations within its normal plane. The magnitude of the rhombic angle θ directly dictates the edge sharpness of the "line-contact damage." When θ=30°, an exceptionally sharp "wedge line-contact damage" configuration is formed. Such an acute linear load can rapidly sever the lattice slip systems within the aluminum alloy, making it highly susceptible to inducing petaling cracking or ductile tearing in the target plate. Cracks propagate rapidly along the impact line, allowing the target plate to fail at an extremely low strain energy cost. However, as θ increases to 90°, the edge becomes blunter, and the initial "line contact" rapidly evolves into a broad face contact. Consequently, the failure mechanism degrades from highly efficient "crack cutting" to "shear plugging," which necessitates significantly greater

energy dissipation, ultimately resulting in a marked decline in terminal ballistic performance.

Table 5. Velocity attenuation rates of the fragments during penetration under various impact velocities ($v_0 \geq 200$ m/s)

Fragment Morphology	Impact velocity v_0 （m/s）						
	200	300	400	500	600	700	800
	Attenuation rate δ_l （%）						
e=0	100	100	85.35	52.53	43.01	38.18	36.01
e=0.4	100	100	71.39	47.19	39.29	35.82	33.14
e=0.8	100	100	56.01	36.65	28.98	25.59	23.38
λ=0.5	100	100	100	69.58	62.91	57.45	56.12
λ=1	100	100	58.99	49.77	44.80	43.77	41.54
λ=2	100	54.93	40.87	33.19	31.50	29.23	31.56
θ=30°	100	100	45.61	29.44	19.73	15.56	12.85
θ=60°	100	100	64.65	41.55	32.19	27.07	23.98
θ=90°	100	100	99.20	59.84	49.02	44.25	42.01

Table 5 presents the respective velocity attenuation rates δ_l of the nine fragment morphologies during the penetration process, evaluated at impact velocities equal to or exceeding their individual perforation thresholds. The mathematical formulation for calculating this attenuation rate is expressed as follows:

$$\delta_l = \frac{v_0 - v_f}{v_0} \tag{3.1}$$

An analysis of the data indicates that the velocity attenuation rates for all fragments exhibit a pronounced nonlinear monotonic decrease with increasing impact velocity, gradually plateauing in the high-velocity regime. Under the constraint of equivalent mass, the penetration energy absorption of the lightweight aluminum alloy target plate demonstrates extreme sensitivity to the geometric morphology of the fragments. On the one hand, an increase in the sectional density significantly mitigates the attenuation of penetration kinetic energy. As the aspect ratio λ increases to 2.0 or the eccentricity e increases to 0.8, the contact area between the fragment and the target diminishes sharply. The consequent surge in localized specific kinetic energy propels a transition in the target's failure mode from high-energy-dissipation global plastic stretching or bending to low-energy-dissipation localized shear plugging. This phenomenon is particularly pronounced for the slender fragment with an aspect ratio λ= of 2.0, which is the first to achieve effective perforation at a critical velocity v_0 of 300 m/s (with the attenuation rate dropping to 54.93%).

On the other hand, the sharpening of the contact interface can maximize the reduction of the target plate's penetration resistance. When the rhombic angle θ is sharpened from 90° to 30°, the attenuation rate of the fragment at an ultra-high velocity v_0 of 800 m/s plummets from 42.01% to 12.85%, which is the lowest among all groups. The underlying physical mechanism is that the extremely sharp wedge-shaped "line contact" generates intense localized stress concentration instantaneously upon impact. This preferentially cuts along the line of action and induces low-strain-energy ductile tearing and petaling cracking in the target plate,

thereby accomplishing armor penetration with optimal mechanical efficiency. The comparative curves of the attenuation rates for the three series and nine morphologies of fragments under different impact velocities are illustrated in Fig. 5.

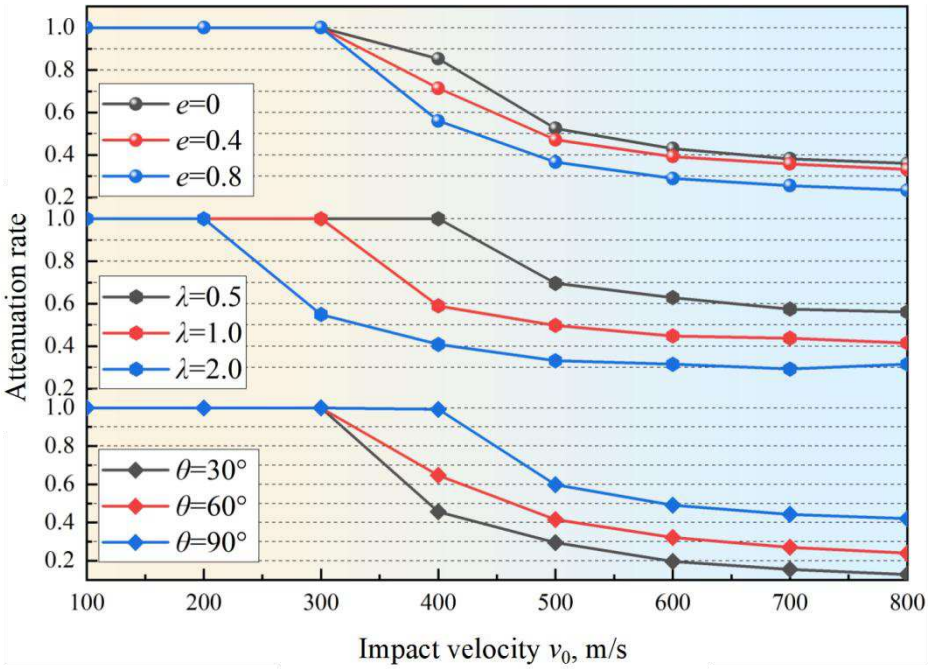


Fig.5. The δ-v_0 curve of fragments.

Observation of the three series of δ-v_0 curves reveals that the penetration attenuation processes of all fragments exhibit highly consistent inverted S-shaped nonlinear evolution characteristics. The entire velocity domain can be clearly divided into three dynamic stages:

Absolute attenuation region: When the impact velocity falls below the respective ballistic limit , the curve presents as a horizontal straight line. At this stage, the target plate remains unperforated, and the initial kinetic energy of the fragment is fully converted into the global plastic strain energy, local failure energy and thermal energy of the target.

Sharp transition region: After exceeding the ballistic limit, the attenuation rate drops abruptly in an exponential manner. A steeper slope indicates higher energy utilization efficiency of the fragment geometry for penetration, and a more fragile critical state of the target against perforation.

High-velocity asymptotic region: When $v_0 \geq 600$m/s, the descending trend of all curves slows down markedly and gradually converges toward a specific constant asymptote.This stabilization fundamentally originates from the transition of the dominant penetration resistance mechanism. Under hyper-velocity impact conditions, the local strain rate of the target is extremely high, and the penetration resistance transitions from being dominated by the quasi-static structural strength of the material to being predominantly governed by target inertia and hydrodynamic drag. In this regime, the energy dissipation required to displace the target material becomes approximately proportional to the square of the impact velocity (v^2). Consequently, the ratio of the dissipated kinetic energy to the initial kinetic energy tends toward a

constant, causing the velocity decay rate (δ) to flatten out. Furthermore, the distinct geometric topologies of the fragments primarily dictate the inertial drag coefficients; hence, different shapes converge to distinctly separated horizontal asymptotes rather than a single unified value, permanently preserving their morphological advantages in overcoming inertial resistance.

The curves of the spherical/ellipsoidal e-series are highly coincident below 300 m/s. However, once exceeding 300 m/s, the three curves diverge in an approximately parallel fashion, with larger e values corresponding to lower curve positions. All e-series fragments feature smooth head curvature, which implies that their incipient energy thresholds for inducing initial yielding and material displacement of the target are similar (all around 300 m/s). Nevertheless, once the penetration channel is formed, the slender ellipsoid with e=0.8, due to its reduced lateral cross-section, experiences significantly lower lateral friction and radial extrusion resistance from the target surface during the tunneling stage compared with the standard sphere (e=0.8). This manifests as a stable equidistant descending pattern on the curves after crossing the ballistic limit.

The curves of the length-to-diameter ratio λ-series exhibit the largest dispersion along the velocity axis. The curve for λ=2.0 completes its steep drop within the velocity range of 200–300 m/s, whereas the curve for λ = 0.5 does not start descending until 400 m/s. This intuitively demonstrates the effect of forced dimensionality reduction from areal damage to point damage. The reduction in cross-sectional area (i.e., increase in λ greatly advances the critical point of shear plugging, enabling the fragment to cross the absolute attenuation region at an extremely low threshold. Meanwhile, the curve for λ = 2.0 consistently remains at the lowest level ($\delta\approx0.3$) throughout the high-velocity section, verifying that slender bodies possess a sustained ballistic advantage in overcoming the inertial resistance of the target.

The rhombic prism grid angle θ-series shows remarkable slope differences in the sharp transition region. In particular, the curve for θ=30° undergoes a precipitous drop in the 300–400 m/s range and approaches the absolute minimum value of the entire plot at 800 m/s. The extremely high stress concentration induced by the sharp wedge-shaped linear edge (θ=30°) causes ductile tearing and cracking of the target within a very short time. This failure mode consumes very little kinetic energy, resulting in an extremely steep gradient variation of the curve. In contrast, the curve for θ=90° tends to be gentle, and its high-velocity asymptote is significantly elevated ($\delta>0.4$), indicating that the obtuse angle blunts the wire-cutting effect and degrades it into a high-energy-consumption areal impact mode.

As can be seen from the dynamic evolution pattern of the curves: in high-velocity impact protection scenarios for lightweight target plates, the geometric sharpness (θ) of the fragment dominates the attenuation slope in the transition region — which determines the energy cutting efficiency at the instant of perforation — whereas the cross-sectional size (λ and e) governs the magnitude of the horizontal shift of the entire attenuation curve toward the low-velocity region as well as the

lower limit of the high-velocity asymptote. This conclusion provides a quantitative ballistic basis for the shape optimization design of high-efficiency damage elements.

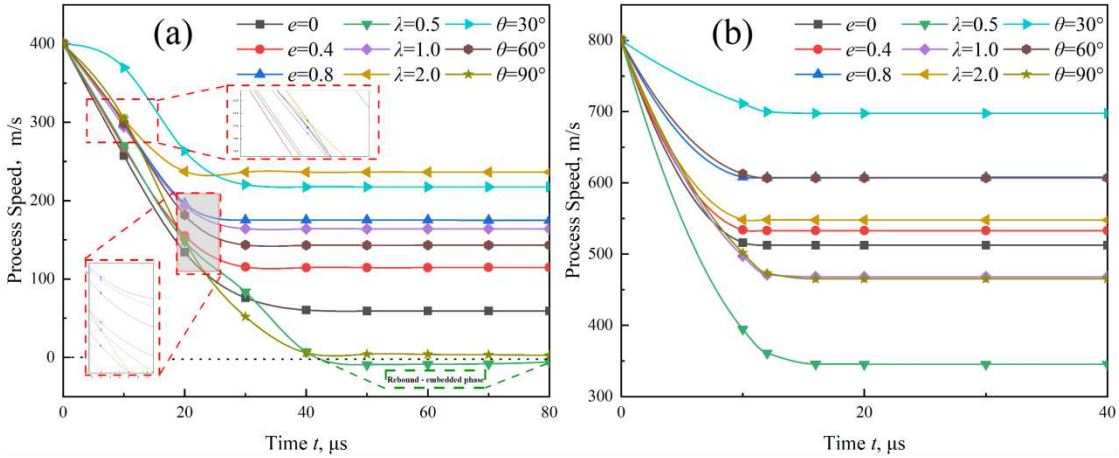


Fig.6. Velocity–time (v–*t*) curves for fragments of various geometries during perforation of the target plate at low and high impact velocities. (a) v–*t* curves at v_0=400m/s(b) v–*t* curves at v_0=800m/s

As observed in Fig. 6(a), at an initial velocity of v_0=400m/s, the impact velocity lies close to the ballistic limits of fragments with various geometries. The coupling between the strain rate effect of the target material and the global structural response reaches its highest complexity, resulting in remarkably distinct temporal behaviors among all groups of v–*t* curves.

For fragments that successfully perforate the target, their velocity gradually levels off within the interval of 20–30 μs, which marks the complete penetration of the fragment through the rear surface of the target and a rapid decay of the resistance force to zero. In contrast, the deceleration process of non-perforating fragments is prolonged beyond 40 μs. A rebound–embedding stage is clearly identified in the figure. Taking the flat cylinder (λ=0.5) or obtuse rhombic fragment (θ=90°) as examples, their velocity curves not only drop to zero at approximately 40 μs but also exhibit slight negative values. From a physical mechanics perspective, this indicates that the large impact surface of the fragment forces the target to undergo extensive global elastic–plastic bending deformation. When the kinetic energy of the fragment is fully dissipated, shear plugging failure is not initiated; the elastic strain energy accumulated in the target is then released via elastic springback, exerting a reverse thrust on the fragment and causing it to be captured by the target or undergo slight rebound. Conversely, fragments with acute-angle linear damage (θ=30°) and slender point damage (e=0.8, λ=2.0) feature small contact areas and extremely high stress concentration. Although their deceleration curves exhibit a certain gradient in the initial stage, they maintain forward penetration throughout the process, effectively avoiding the high energy dissipation trap induced by global deformation of the target.

Further observation of Fig. 6(b) shows that when the impact velocity increases to v_0=800m/s, all fragments possess sufficient kinetic energy to perforate the target, and the penetration mechanism transforms into a hydrodynamics- and shear-dominated mode under local high strain rates. Compared with the low-velocity regime, the entire penetration process at 800 m/s is significantly compressed. All curves complete the

steep velocity drop and enter a stable residual velocity stage within 10–15 μs. This indicates that under hypervelocity conditions, adiabatic shear localization and even melting failure occur in the target material instantaneously upon contact, and the fragment cuts through the target in an extremely transient manner.

During the main penetration phase of 0–15 μs, the absolute values of the curve slopes follow a precise topological order: areal damage fragments exhibit the steepest slope, followed by point damage fragments, while acute-angle linear damage fragments show the gentlest slope. For the extreme linear damage case (θ=30°), the curve descends most gently. The sharp wedge-shaped cutting edge exhibits an effect analogous to a hot knife through butter under ultra-high strain rates, tearing the material lattice instantaneously along the line of action. The transient resistance, reflected by the slope, is extremely small, resulting in a residual velocity as high as approximately 700 m/s. For the areal damage configuration with a large cross-section, fragments with a large frontal area must overcome not only the dynamic yield strength of the material but also the substantial inertial resistance of the target material. Under high-velocity impact, the hydrodynamic resistance required to displace target material of equal area is proportional to the square of the velocity, leading to an instantaneous and drastic velocity loss and a precipitous drop in the curve.

3.2. Analysis of ballistic limit speed

Figure 7 depicts the ballistic limit velocity V_{bl} for nine distinct fragment geometries penetrating a 5 mm-thick target plate. As a macroscopic critical metric, V_{bl} characterizes both the protective performance of the target plate and the penetration potency of fragments. The extreme value distribution and stepwise gaps across configurations shown in the figure further quantitatively corroborate the decisive role of topological contact dimension reduction in enhancing fragment penetration efficiency.

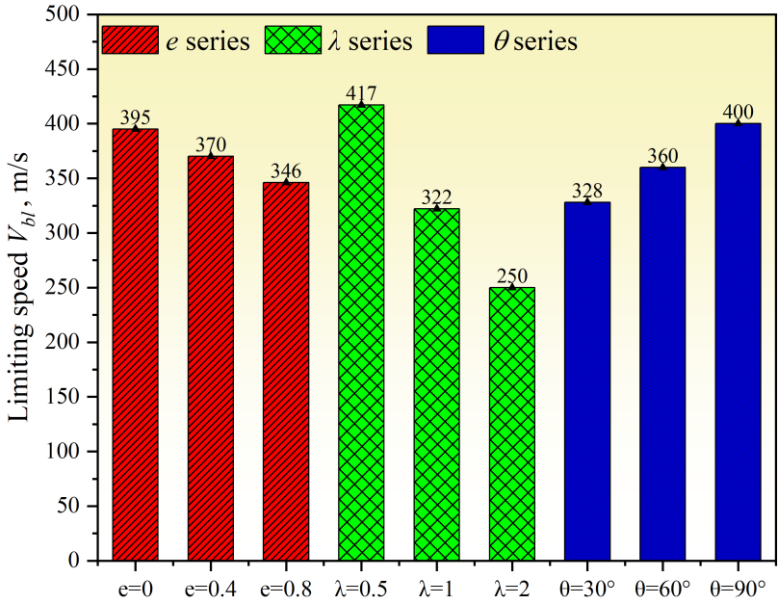


Fig.7. Ballistic limit velocity V_{bl} for fragments of various geometries during penetration of the 5-mm-thick target plate.

The data of the e-series fragments exhibit a relatively tight distribution, reflecting the stable radial displacement effect under the point damage mechanism. The ballistic limit decreases from 395 m/s for the standard sphere to 346 m/s for the slender ellipsoid (e=0.8). Although the reduction of approximately 12.4% is less pronounced than that of the length-to-diameter ratio series, it still follows the beneficial trend of increasing sectional density. It is noteworthy that even though the ellipsoid with e=0.8 shares similar slenderness characteristics with the λ=2.0 configuration, its V_{bl} (346 m/s) remains considerably higher than that of the λ=2.0 case (250 m/s). Mechanistically, this indicates that the initial micro-surface impact of the slender flat-ended cylinder is still more efficient at inducing adiabatic shear plugging than the ductile cavity expansion triggered by the smooth nose of the ellipsoid.

The λ-series fragments show the widest data span among the three groups, which perfectly illustrates the ballistic benefit of forced dimensionality reduction from areal damage to point damage. At λ=0.5, the fragment presents typical areal damage features. The large impact cross-section induces the most extensive global bending and membrane stretching of the 2A12 aluminum alloy target, driving the ballistic limit up to the maximum value of 417 m/s across all configurations. This implies that under equal mass, wide-cross-section fragments yield the lowest penetration efficiency, due to the longest energy dissipation path and the highest energy absorption of the target material. As λ increases to 2.0, the impact behavior shifts toward point damage and the sectional density reaches its peak. Accordingly, the ballistic limit plummets to the group minimum of 250 m/s, corresponding to a reduction of up to 40%. This substantial threshold difference signifies from an engineering perspective that slender fragments can achieve shear plugging of lightweight armor at an extremely low initial velocity threshold, converting the energy originally consumed to overcome global deformation of the target into effective kinetic energy for direct penetration.

The stepwise variation of the θ-series quantifies the contribution of the stress concentration effect to the penetration threshold. The acute-angle rhombic fragment (θ=30°), representing extreme linear damage, features a wedge-shaped cutting edge with ultra-high geometric sharpness and yields a ballistic limit of only 328 m/s. Such sharp line contact induces intense local shear instability instantaneously upon impact, causing the target to be cut and torn before extensive plastic flow can develop. As the grid angle blunts to a square shape (θ=90°), the line contact degrades and approximates planar impact, which requires the target to absorb more deformation energy. The ballistic limit consequently rises to 400 m/s, with penetration resistance nearly equivalent to that of the flat cylinder (λ=0.5).

Figure 8 presents the stress contours of target plate damage induced by fragment penetration. The temporal evolution of stress contours for nine equal-mass shaped fragments penetrating a 5-mm-thick 2A12 aluminum alloy target at the ballistic limit velocity profoundly reveals the governing mechanism of fragment topological geometry on the energy dissipation path throughout the full penetration cycle.

The entire penetration process strictly follows five characteristic dynamic stages, yet distinct geometric configurations give rise to remarkable differences in the

duration of each stage and the stress wave response within the target plate. In Stage I, defined by elastic contact between the two surfaces accompanied by local yielding, and in the early phase of Stage II featuring shear fracture and incipient ductile hole enlargement, the nose profile of the fragment exerts a decisive dominant effect. Configurations represented by the large length-to-diameter ratio (λ=2.0) and acute-angle rhombic fragment (θ=30°) possess a minute contact area or an extremely sharp wedge-shaped cutting edge upon impact. These features rapidly disrupt the load-bearing network of the target material via intense localized stress concentration, enabling direct transition to the local shear and ductile tearing of Stage II with negligible large-scale elastic energy release or global yielding of the target. Conversely, areal-damage fragments such as the flat cylinder (λ=0.5) and square prism (θ=90°) induce broad planar compression waves at the initial contact stage. The high-stress zone propagates laterally over an extensive range inside the target, forcing severe global plastic bending of the plate. This energy-intensive structural response significantly retards the formation of an effective perforation.

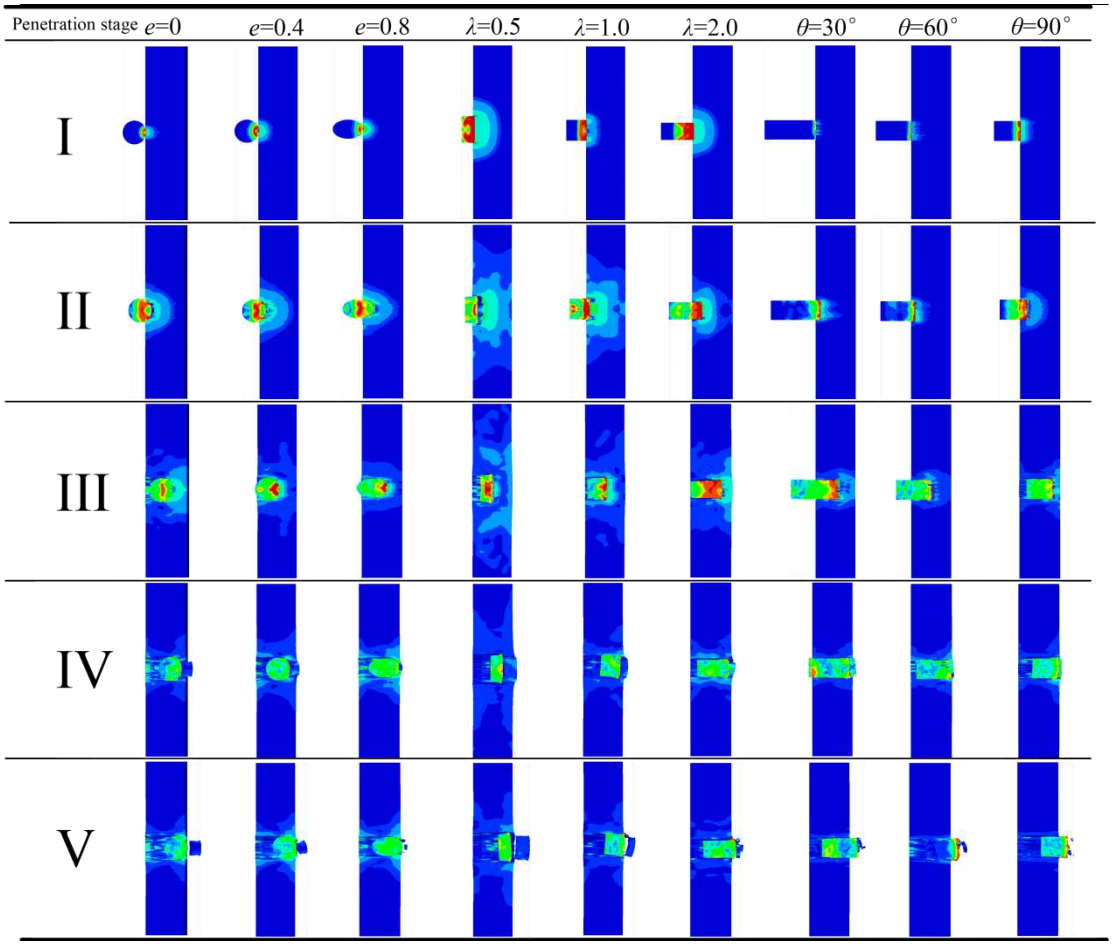


Fig.8. Schematic illustration (cross-sectional views) of the penetration process of nine fragment geometries into the target plate at the ballistic limit.

As penetration depth increases, the process enters Stage III, characterized by long-stroke penetration within the target and localized stress intensification surrounding the penetration tunnel. At this stage, the slender ellipsoid (e=0.8) and the high length-to-diameter ratio cylinder exhibit superior ballistic efficiency. Their

reduced cross-sections confine the high-stress zone strictly within the narrow channel adjacent to the projectile sidewall, effectively suppressing the diffusive dissipation of stress waves into surrounding non-target regions. In contrast, a substantial plastic wave front accumulates ahead of wide-cross-section fragments, rendering radial material displacement extremely difficult and causing a sharp escalation in frictional and hydrodynamic resistance.

When penetration advances to Stage IV — complete shearing of the internal plug, forward plug displacement, and rear-surface perforation of the target — the kinetic energy disparity accumulated from differing failure mechanisms in preceding stages finally becomes manifest. Acute-angle line-contact fragments shear off only a minute plug or even no distinct plug mass, while slender point-contact fragments smoothly eject a micro-scale plug with a width matching their small diameter, resulting in minimal rear-surface perforation resistance. To achieve full perforation, flat fragments must forcibly tear and displace a large plug of considerable volume and thickness, which nearly exhausts their entire kinetic energy reserve at the ballistic limit.

Finally, at Stage V when complete fragment perforation is achieved and the penetration process terminates, a definitive conclusion can be drawn: topological optimization successfully enforces a transition from the energy-intensive wide-range plugging and global deformation mode to a low-energy localized shear and micro-hole-enlargement mode. This constitutes the mesomechanical essence underlying the ability of slender and acute-angle fragments to defeat lightweight armor at a lower kinetic energy threshold.

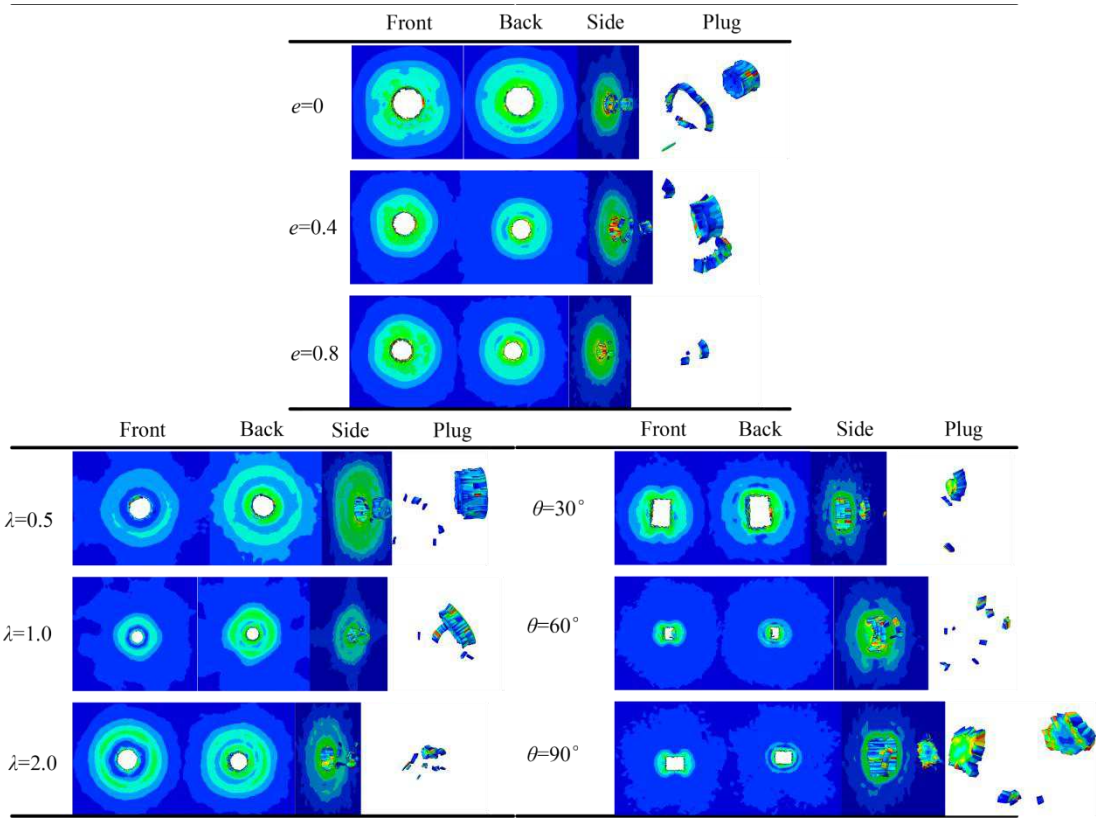


Fig.9. Morphologies of target damage and shear plugs induced by fragments at the ballistic limit.

(a) *e*-series fragments (b) λ-series fragments (c) θ-series fragments

As revealed by the target damage and shear plug morphologies produced by fragments at the ballistic limit in Fig.9, fragments with distinct topological geometries exhibit drastically different energy absorption mechanisms and fracture characteristics under this critical condition.

The underlying core mechanism is that as the fragment geometry undergoes dimensionality reduction from areal contact to line contact and point contact, the dominant failure mode transitions from energy-intensive structural response to low-energy localized failure. Representative of areal damage, flat cylinder and square prism fragments feature large, blunt contact surfaces that induce intense broad stress waves immediately upon impact, driving extensive global plastic bending of the target plate. To achieve full perforation, these fragments must forcibly tear and displace a large, intact massive shear plug; such global coupling effects dissipate a major fraction of the fragment's kinetic energy.

Conversely, point damage configurations such as slender cylinders and ellipsoids leverage their minimal frontal area to strictly confine the stress concentration zone within the narrow channel adjacent to the projectile sidewall, effectively suppressing lateral energy dissipation. Consequently, only a tiny shear plug is smoothly ejected, and in some cases no distinct plug is formed at all. For the acute-angle rhombic prism, its sharp line-contact cutting edge disrupts the target's load-bearing network via an ultra-high stress gradient at the instant of impact. This triggers low-energy ductile tearing and petal-like cracking, allowing complete penetration to occur even without the formation of a full plug.

This pronounced discrepancy in damage morphologies provides fundamental physical evidence that reducing the cross-sectional area and sharpening the contact front constitute the most effective strategies for improving fragment penetration efficiency and lowering the kinetic energy threshold required for target perforation.

3.3 Analysis of the Mechanism of Target Thickness Effect

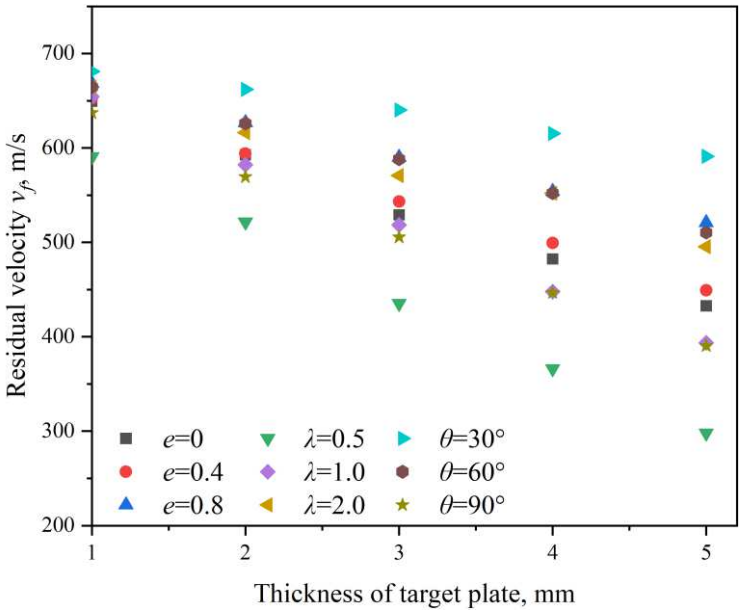


Fig.10. Residual velocity of fragments after penetration for different target thicknesses at v_0=800m/s.

Figure 10 presents the scatter distribution of fragment residual velocity versus target thickness (1–5 mm) under high-velocity impact at 800 m/s. At this high kinetic energy baseline, a distinct thin-target convergence effect manifests in the early penetration stage: for 1–2 mm thin targets, the absolute kinetic energy of the fragments is overwhelmingly dominant, and the structural resistance of the target plate is not fully activated. Accordingly, the residual velocities of all fragment geometries cluster tightly above 700 m/s.

However, as penetration proceeds over a longer stroke and target thickness increases to 3–5 mm, the ballistic advantage of topological dimensionality reduction becomes pronounced and gives rise to data divergence. In this regime, inertial damping and hydrodynamic resistance of the target material dominate the penetration process. Fragments representing acute-angle linear damage (θ=30°) and slender point damage (λ=2.0)) effectively maintain a narrow localized shear channel by virtue of their extremely small frontal cross-sections and high-gradient stress concentration, retaining a high residual velocity of 600–700 m/s after perforating the 5-mm-thick target. By contrast, flat areal-damage fragments (λ=0.5) suffer a sharp decline in residual velocity to approximately 350 m/s, as they must overcome substantial wide-range material displacement resistance. This intuitively demonstrates the extreme sensitivity of energy dissipation in thick targets to fragment cross-sectional properties in the hypervelocity regime.

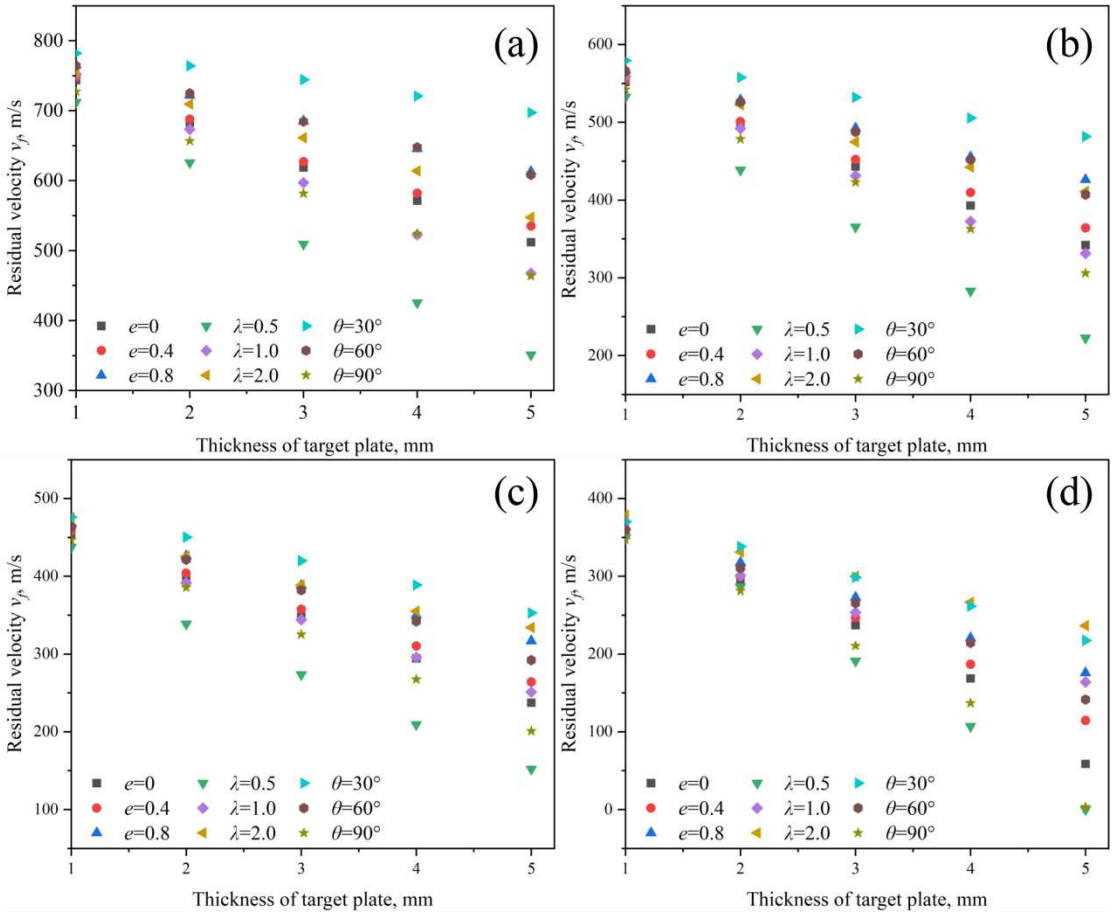


Fig.11. Residual velocity after penetration of target plates with different thicknesses at initial velocities ensuring perforation for all fragment geometries (v_0≥400m/s). (a)v_0=700m/s(b)v_0=600m/s(c)v_0=500m/s(d)v_0=400m/s

Figure 11 further reveals the coupled penetration evolution behavior of target thickness and fragment geometry as the initial impact velocity decreases stepwise from 700 m/s to the critical low value of 400 m/s. With the stepwise attenuation of initial impact kinetic energy, the data divergence effect in the thick-target range is drastically amplified, and the global structural stiffness of the lightweight target plate, together with the energy-intensive plastic bending mechanism, begins to exert a strong governing effect.

Examination of the dynamic evolution from Figs. 11(a) to 11(d) indicates that, under the low-velocity condition of 400 m/s against a 5-mm aluminum alloy target, fragments with λ=0.5 and θ=90° feature excessively large initial impact areas. As a result, their kinetic energy is depleted by global target deformation and the formation of a massive shear plug before effective localized shear can be established, leading to a complete loss of residual velocity and fragment retention within the target. In contrast, fragments with θ=30° and λ=2.0 still achieve effective perforation at velocities exceeding 200 m/s.

This progressive trend confirms a key mechanical conclusion: the lower the impact velocity and the thicker the protective armor, the stronger the target's amplification effect on energy-intensive failure modes. Only by slendering and sharpening the fragment geometry to forcibly preclude large-scale global deformation of the target can the ballistic limit of thick targets be successfully overcome under low-kinetic-energy constraints.

As depicted by the bar chart of penetration energy dissipation in Fig.12, in terms of the overall evolutionary trend, the energy dissipated by fragments of all geometries during target perforation increases strictly and monotonically with target thickness, regardless of whether the impact velocity is 800 m/s (high velocity) or 400 m/s (medium-low velocity). Meanwhile, for a given target thickness, the absolute energy dissipation under 800 m/s high-velocity impact is markedly higher than that at 400 m/s.

With regard to topological geometry, the magnitude of energy dissipation is strictly governed by the contact characteristics of the fragments, and the performance ranking of configurations remains highly consistent across different velocity regimes. Configurations with the largest frontal cross-sectional area and the bluntest contact surfaces consistently exhibit the highest penetration energy dissipation, confirming that the wide-range plugging and global deformation they trigger consume a disproportionate amount of kinetic energy. By contrast, slender cross-sectional configurations and those featuring sharp cutting edges yield the lowest energy dissipation during penetration.

These quantitative findings directly validate the foregoing theoretical mechanism: enhancing the slenderness and sharpness of fragment geometry can effectively localize the penetration mode and substantially reduce the energy expended in

overcoming global structural deformation of the target, thus enabling complete perforation with minimal energy cost.

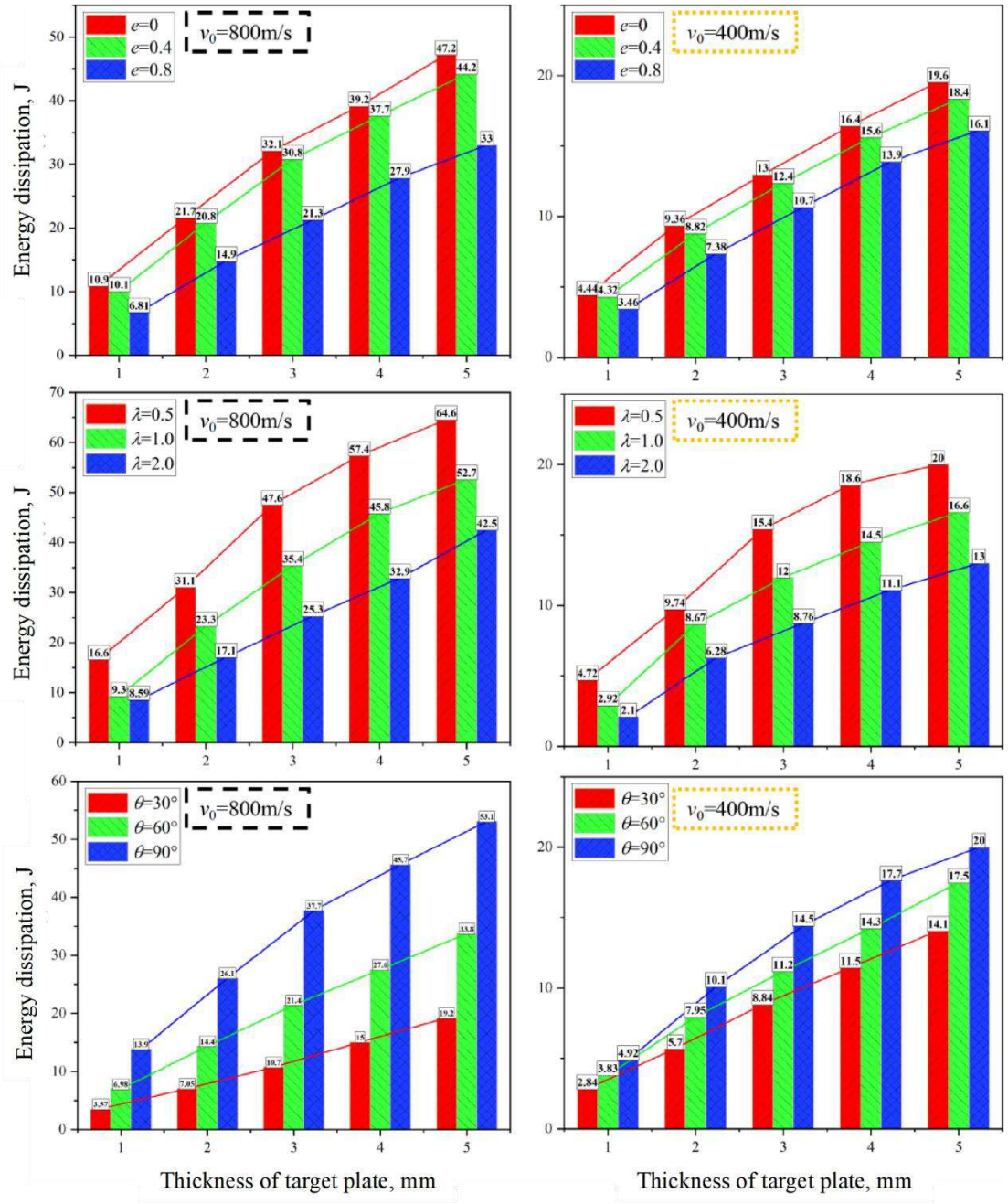


Fig.12. Energy dissipation of fragments during target penetration for different target thicknesses at v_0=800m/s and 400m/s.

3.4 Analysis of the Influence Mechanism of Impact Attitude

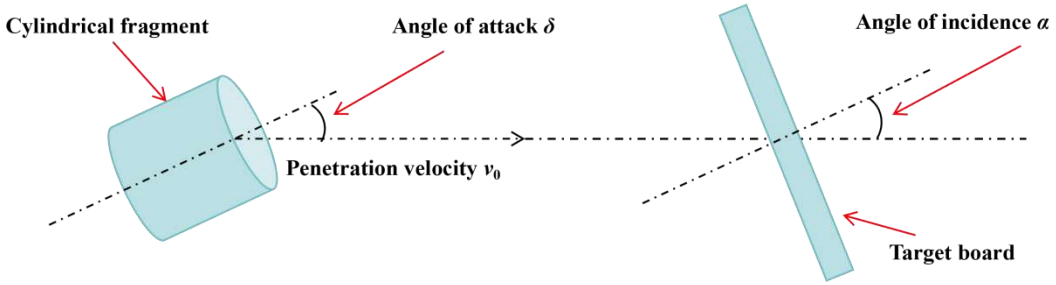


Fig.13. Schematic illustration of the definitions of angle of incidence α and angle of attack δ.

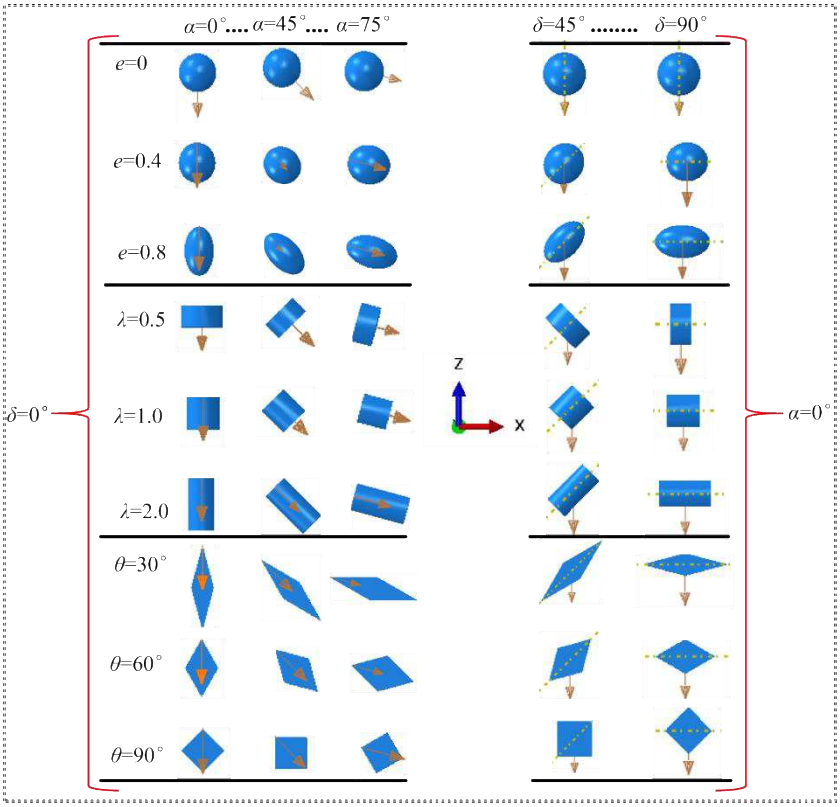


Fig.14. Schematic illustration of different impact attitudes of fragments.

In view of the susceptibility of fragments to attitude deflection during actual dispersal and aerodynamic flight, which gives rise to randomness and instability in impact conditions (as conceptually illustrated in Fig.13), this study conducts extended numerical simulations for non-ideal scenarios based on the previously derived laws of ideal normal penetration. Taking a 3-mm-thick 2A12 aluminum alloy plate as the reference target, the angle of incidence α and angle of attack δ are independently introduced as variables to systematically investigate the effects of these two single-mode attitude deflections on the penetration performance of nine topologically distinct fragment geometries. Figure 14 shows schematic diagrams of different impact attitudes for the three fragment series. Figure 15 presents the residual velocity curves of fragments penetrating the 3-mm-thick target at v_0=500m/s under various angles of incidence α.

Observation of the overall characteristics of the three sets of curves in Fig.15 reveals that the residual velocities of all nine fragment types exhibit a notable decreasing trend with increasing angle of incidence α. Within the range of α=0° to 45°, the residual velocity declines relatively gently, as the substantial kinetic energy reserve of the fragments effectively compensates for the increase in effective target thickness. However, once the critical angle of α=45° is exceeded, all curves drop precipitously, with pronounced divergence among different topological configurations. Taking the λ=0.5 cylinder and θ=90° rhombic prism, which represent areal damage, as examples, their residual velocities approach or reach zero at 60°, demonstrating

extremely high sensitivity to oblique impact conditions. In contrast, the slender cylinder with λ=2.0 and the acute-angle rhombic prism with θ=30° retain considerable armor-piercing kinetic energy at 60° by virtue of their high sectional density and sharp leading edges, confirming the ballistic advantage of topological dimension reduction design in resisting oblique penetration.

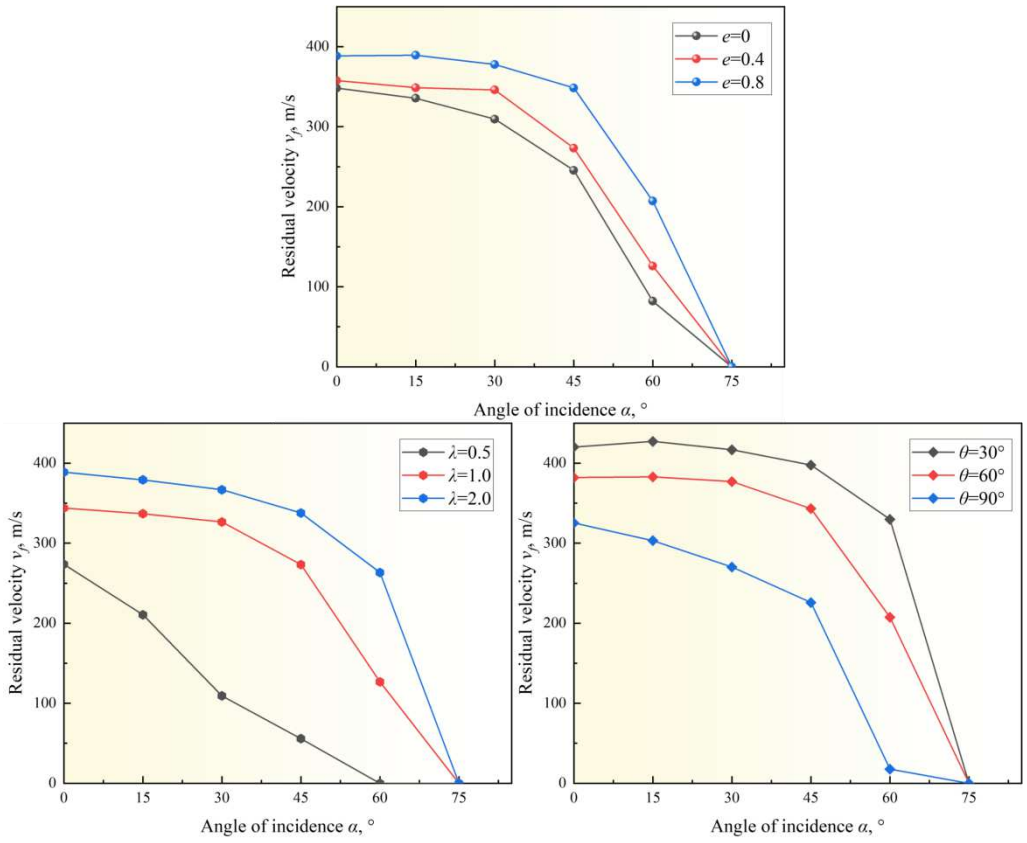


Fig.15. Residual velocity curves of fragments after target penetration under different angles of incidence α at v_0=500m/s.

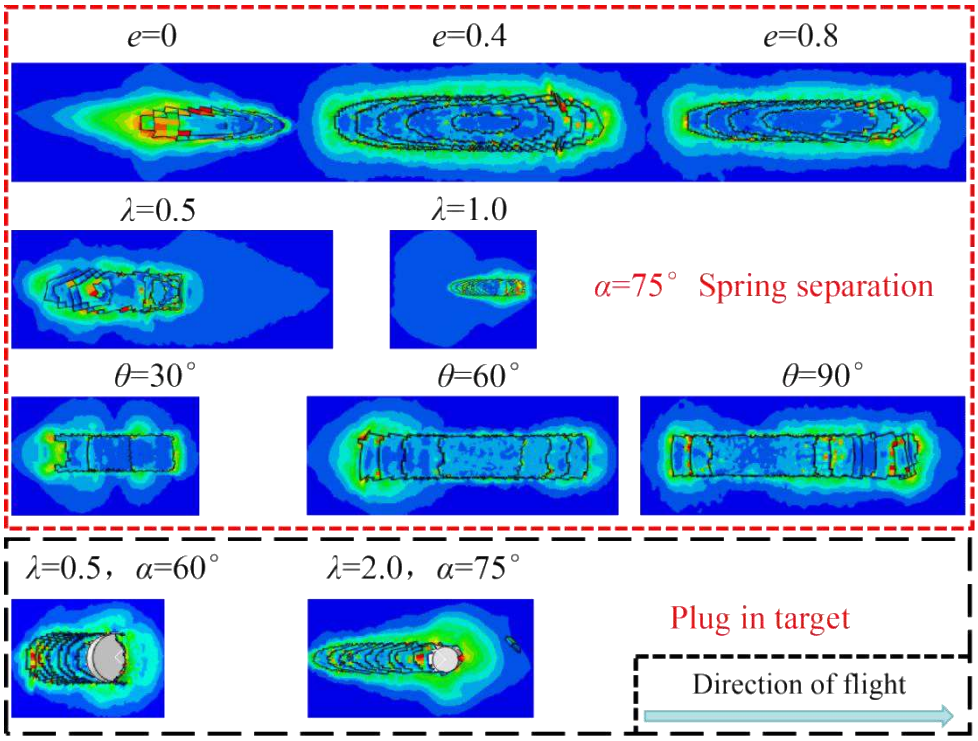


Fig.16. Failure modes of fragment-induced damage under large angles of incidence α.

When the angle of incidence increases to 60° and 75°, the fragment penetration mode evolves completely from ideal perforation to damage failure, shifting from perforation to energy-intensive embedment within the target or ricochet and departure. The final physical outcome is primarily determined by the geometric and topological characteristics of the contact leading edge. These damage failure modes are illustrated in Fig.16, which depicts the failure modes of target penetration and damage by fragments at different angles of incidence α. Effective perforation is achieved at α=0°, 15°, 30° and 45°, while only the fragment with λ=0.5 fails to penetrate at α = 60°. Analysis of the figure indicates that fragments with sharp cutting edges, such as the θ=30° configuration, exert a strong chiseling effect at the extreme grazing angle of 75°. Although they can barely penetrate the armor, they effectively cut the surface layer of the target. Due to the interplay between lateral sliding resistance and the oblique angle, the fragments undergo noticeable deflection and separation after plowing a narrow and long damage groove, exhibiting a ricochet and separation morphology. For areal-contact configurations such as λ=0.5 or θ=90°, their large frontal area subjects them to intense asymmetric retardation and overturning moments during oblique penetration. Under the action of strong surface pressure and shear friction, the fragments are usually completely locked within the target immediately after penetrating the surface layer as their kinetic energy is exhausted, forming a typical embedment failure mode.

In summary, variation in the angle of incidence not only increases the effective target thickness, but also determines whether the fragment ultimately undergoes sliding ricochet or embedment failure by altering the topological dimension of the contact interface. Slender and sharp geometric design represents a key approach to mitigating performance loss in large-angle oblique penetration.

Figure 17 presents the residual velocity curves under different angles of attack. The data indicate that, unlike the angle of incidence which alters the effective target thickness, the introduction of the angle of attack δ does not physically change the trajectory of the fragment; instead, it directly modifies the initial contact topological morphology and projected frontal area at the instant of target impact. At an initial velocity v_0 of 500 m/s, the residual velocity versus angle of attack curves vividly demonstrate the dynamic transformation effect of damage mechanisms induced by the spatial tumbling of fragments.

First, as a benchmark for topological symmetry, the standard sphere (e=0) maintains a strictly constant residual velocity across the entire range of angles of attack, which perfectly corroborates its isotropic contact characteristics. However, for shaped fragments with pronounced anisotropic characteristics, attitude deflection leads to a drastic and dramatic reversal of ballistic performance.

On the one hand, slender point-damage configurations (e.g., the slender ellipsoid with e=0.8 and acute-angle line-damage configurations (e.g., the rhombic prism with θ=30°), which originally exhibit superior penetration performance under the normal attitude (δ=0), experience a substantial and abrupt decline in residual velocity as the angle of attack increases toward 90°. This occurs because during large-angle lateral impact, their originally small frontal cross-sections or sharp cutting edges are fully concealed, and the fragments instead strike the target with their broad lateral profiles. This forced topological dimensionality upgrade—from efficient point/line cutting to energy-intensive areal impact—dramatically elevates the global deformation resistance of the target plate, causing these configurations to even become the least penetrative among all groups under lateral impact (θ=90°).

On the other hand, a nonlinear response is observed for the flat cylinder (λ=0.5) and the equal-length cylinder (λ=1.0). These areal-damage fragments, which exhibit high energy dissipation and low residual velocity at 0° angle of attack due to their blunt flat end faces, undergo an extremely intense and anomalous rise in residual velocity when the angle of attack deflects into the range of 45°–60°, with the peak value even exceeding 600 m/s. Mechanistically, this arises because at a specific inclination angle, the cylinder contacts the target precisely with the sharp right-angle edge of its end face, instantaneously converting the originally inefficient wide-range areal compression into extremely sharp point/line chiseling and cutting. This topological dimensionality reduction effect, accidentally triggered by attitude deflection, maximally avoids global plastic bending of the target plate.

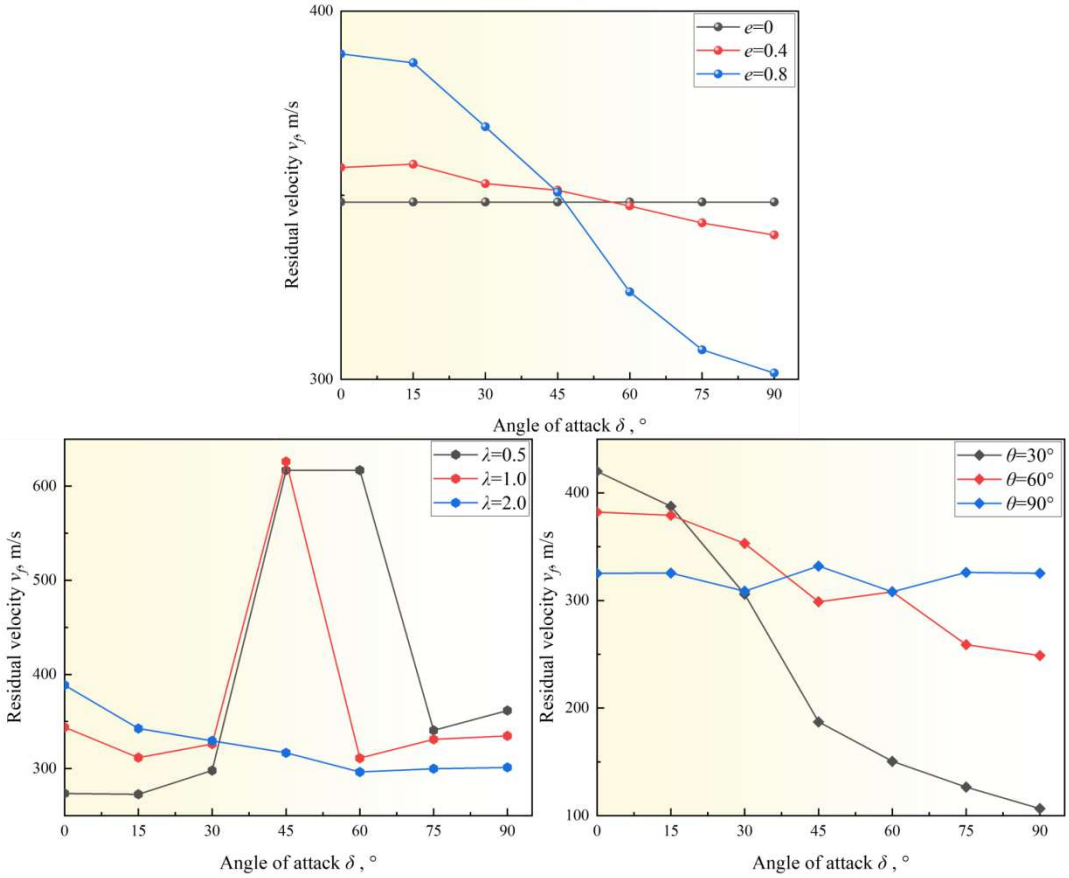


Fig.17. Residual velocity curves of fragments after target penetration under different angles of attack δ at .

The above findings profoundly indicate that under actual dispersal and aerodynamic tumbling conditions, the equivalent contact boundary between the fragment and the target undergoes complex dynamic transitions among point, line and areal modes. A single fragment geometry optimized solely for the ideal normal attitude is highly prone to a sharp degradation in penetration performance when subjected to large-yaw impact. The normalized residual velocity (NRV) curves under different impact attitudes at v_0=500m/s are shown in Fig.18.

Under different angles of incidence (left panel), the NRV curves intuitively quantify the ability of each configuration to resist the surge in effective target thickness and lateral sliding resistance. The flat cylinder with λ=0.5, representing extreme areal damage, exhibits the weakest stability against oblique penetration, with its NRV declining almost linearly and rapidly from the onset of deflection. In contrast, the rhombic prism with θ=30°, which features sharp cutting edges, demonstrates outstanding anti-yaw retardation performance. Its NRV remains at a very high level across the wide oblique penetration range of 0°–45°, further verifying the decisive role of the chiseling effect induced by line contact in stabilizing the penetration axis and suppressing performance degradation.

Under different angles of attack (right panel), the NRV curves profoundly reveal the extremely nonlinear characteristics of the dynamic transition of damage topological dimensions during the three-dimensional tumbling of fragments. The most

anomalous phenomenon in the figure is the extraordinary armor-piercing gain of 150% to 220% exhibited by the curves of λ=0.5 and λ=1.0 in the 45°–60° range. The mechanical essence lies in the fact that these two flat-headed areal-contact fragments, which are extremely inefficient under normal impact conditions, strike the target precisely with their right-angle edges due to attitude inclination. This accidentally triggers point/line dimensionality reduction at the contact interface, thereby avoiding global bending and resulting in penetration capacity under this attitude far exceeding the baseline value of normal flat-headed impact.

Conversely, for the acute-angle rhombic prism (θ=30°) and high-length-to-diameter-ratio cylinder (λ=2.0), which are specially optimized for normal penetration, the sharp leading edges are completely concealed under lateral impact with the angle of attack approaching 90°. The frontal impact surface is forced to upgrade dimensionally to broad lateral areal contact, causing their NRV to drop sharply to 30% or even less of the baseline value. Only the standard sphere (e=0) maintains a constant relative efficiency of 100% across the entire angle-of-attack range due to its absolute spatial symmetry.

The geometric design of fragments essentially seeks an optimal balance between ultimate penetration power and ballistic attitude robustness. Extreme topological dimensionality reduction (extremely slender or sharply edged configurations) can perforate armor with minimal energy consumption, yet exhibits extremely low tolerance to aerodynamic tumbling. In practical unguided flight scenarios, compromised configurations such as moderately elongated geometries, which balance low-energy frontal material displacement and isotropic characteristics, are required to deliver the most robust comprehensive damage performance under complex and random dynamic impact conditions.

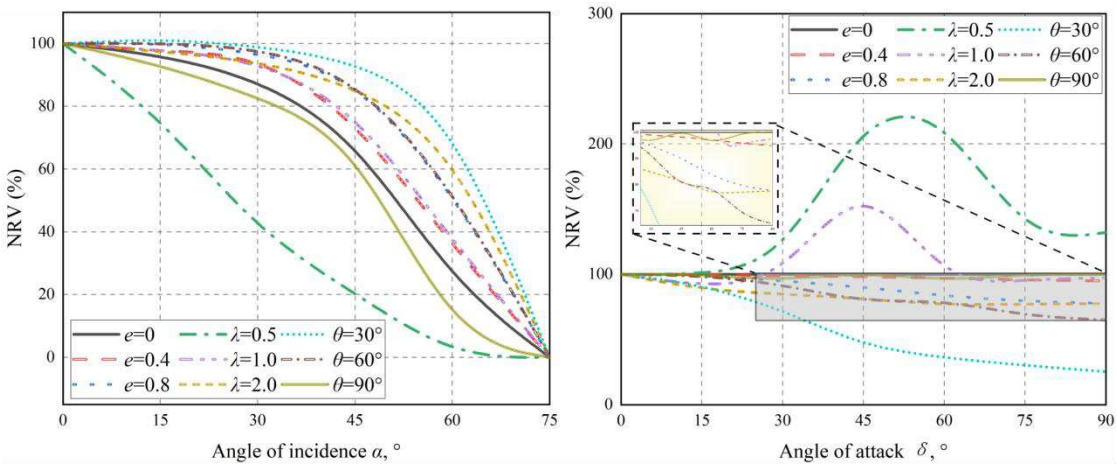


Fig.18. NRV curves of fragments under different impact attitudes at v_0=500m/s.

4. CONCLUSIONS

In this study, explicit dynamic numerical simulations are conducted to reveal the mechanical evolution law of shaped fragments penetrating 2A12 aluminum alloy targets under complex impact attitudes and multi-variable coupling conditions. Based on the theory of topological damage, the core conclusions are drawn as follows:

1) The topological dimension of the initial contact interface is the fundamental factor determining the penetration efficiency and failure mode of the target. The dimensionality reduction of fragment contact morphology from areal contact to point/line contact suppresses global plastic bending and membrane stretching of the target, induces localized adiabatic shear plugging and ductile tearing, and significantly reduces kinetic energy dissipation and ballistic limit velocity.

2) Penetration energy dissipation is highly sensitive to the coupling effect of fragment topological morphology, initial kinetic energy and target thickness. The energy dissipation difference among configurations is masked under high-velocity thin-target conditions, but is exponentially amplified under low-velocity thick-target conditions. Elongating and sharpening the fragment geometry is a decisive mechanical approach to break through the ballistic limit of thick targets under low-kinetic-energy constraints.

3) Under oblique penetration conditions, the geometric sharpness of the fragment leading edge determines the final damage failure mode. Sharp-edged configurations can stabilize the penetration axis and overcome sliding resistance via the chiseling effect, significantly delaying ricochet. Flat-headed configurations, subjected to asymmetric retarding moments, are prone to kinetic energy depletion at the target surface and suffer from embedment failure.

4) Fragment penetration efficiency exhibits strong nonlinearity with angle-of-attack deflection, reflecting the dynamic transition mechanism of damage topological dimensions. Slender and sharp configurations deliver excellent performance under normal impact, but their penetration efficiency declines sharply under lateral impact as the frontal surface is upgraded to areal contact. Therefore, fragment design must balance ultimate penetration power and attitude robustness. A moderately elongated compromise configuration can achieve more stable comprehensive damage performance.

FUNDING

This work was supported by ongoing institutional funding. No additional grants to carry out or direct this particular research were obtained.

CONFLICT OF INTEREST

The authors declare that they have no conflicts of interest.

REFERENCES

[1] Wu Y, Lu W, Yu Y,et al.Penetration Mechanics of Finite -Thickness Aluminum Alloy Plates: A Review of High-Strain -Rate Behavior and Predictive[J].Mechanics of solids, 2025(4): 60. https://doi.org/10.1134/S0025654425601624.

[2] Hao, B., Zheng, H., Cui, Y. et al. Study of the Penetration Performance of Small Blunt Projectiles Against 6061-T6 Aluminum Plates. Mech. Solids 60, 6068–6085 (2025). https://doi.org/10.1134/S0025654425604410

[3] S.K. Sundaram, A.G. Bharath, and B. Aravind, Influence of Target Dynamics and Number of Impacts on Ballistic Performance of 6061-T6 and 7075-T6 Aluminum Alloy Targets, Mech. Based Des. Struct. Mach., 2022, 50(3), p 993–1011.

https://doi.org/10.1080/15397734.2020.1738245
[4] R. Saravanakumar, T. Rajasekaran, and C. Pandey, “Underwater friction stir welded armour grade AA5083 aluminum alloys: experimental ballistic performance and corrosion investigation,” J. Mater. Eng. Perform. 32(22), 10175–10190 (2023).
https://doi.org/10.1007/s11665-023-07836-2
[5] F. Min, K. Gao, W. Wei, et al., “Ballistic resistance of 7XXX laminate aluminum alloy plates and base alloys subjected to different projectiles,” Int. J. Impact Eng. 191, 104998 (2024).
https://doi.org/10.1016/j.ijimpeng.2024.104998
[6] Hong D, Li W, Zheng Y, Jiang N, Zhang K, Liu Z, Jiang Y. Study on Bulge State of PCrNi3MoV Target Plates Penetrated by Square Fragments. Applied Sciences. 2022; 12(14):6987.
https://doi.org/10.3390/app12146987
[7] Xu, S., Liu, M., Yang, J. et al. Analysis on mechanism and damage mode of cylindrical fragments penetrating into protective tank: fragment penetration test and numerical simulation. J Braz. Soc. Mech. Sci. Eng. 47, 191 (2025). https://doi.org/10.1007/s40430-025-05482-4
[8] Zhu, F.L.; Chen, Y.; Zhu, G.L. Numerical simulation study on penetration performance of depleted Uranium (DU) alloy fragments.Def. Technol. 2021, 17, 50–55.
https://doi.org/10.1016/j.dt.2020.01.002
[9] K. Senthil, M. A. Iqbal, B. Arindam, et al., “Ballistic resistance of 2024 aluminium plates against hemispher-ical, sphere and blunt nose projectiles,” Thin-Wall. Struct. 126, 94–105 (2018).
https://doi.org/10.1016/j.tws.2017.02.028
[10] M. Rodriguez-Millan, D. Garcia-Gonzalez, A. Rusinek, et al., “Perforation mechanics of 2024 aluminium protective plates subjected to impact by different nose shapes of projectiles,” Thin-Wall. Struct. 123, 1–10(2018).
https://doi.org/10.1016/j.tws.2017.11.004
[11] Liu, T.L., Xu, Y.X. & Wang, Y.F. Oblique Penetration of Spherical Projectile into Low-Carbon Steel Target: Experiment, Theory, 3D Penetration Model. Mech. Solids 58, 2295–2318 (2023).
https://doi.org/10.3103/S0025654423601039
[12] Xin Liu, Yongjun Deng, Ken Wen, Yong Yao, Jetting and shock wave during oblique hypervelocity impact of spherical projectile, Journal of Mechanics, Volume 40, 2024, Pages 281–298.
https://doi.org/10.1093/jom/ufad012
[13] Li, Y., Zhao, J., Liu, H. et al. Petal failure models of thin aluminum alloy plate penetrated by conical projectile nose. Mech. Solids 57, 427–450 (2022).
https://doi.org/10.3103/S0025654422020170
[14] Gupta N K, Iqbal M A, Sekhon G S. Effect of projectile nose shape, impact velocity and target thickness on the deformation behavior of layered plates[J]. International Journal of Impact Engineering, 2008, 35(1): 37-60.

https://doi.org/10.1016/j.ijimpeng.2006.11.004
[15] Gupta N K, Iqbal M A, Sekhon G S. Effect of projectile nose shape, impact velocity and target thickness on deformation behavior of aluminum plates[J]. International Journal of Solids and Structures, 2007, 44(10): 3411-3439. https://doi.org/10.1016/j.ijsolstr.2006.09.034
[16] K. Senthil, M. A. Iqbal, B. Arindam, et al., "Ballistic resistance of 2024 aluminium plates against hemispher-ical, sphere and blunt nose projectiles," Thin-Wall. Struct. 126, 94–105 (2018). https://doi.org/10.1016/j.tws.2017.02.028.
[17] N. Levy and W. Goldsmith, "Normal impact and perforation of thin plates by hemispherically-tipped projec-tiles—II. Experimental results," Int. J. Impact Eng. 2 (4), 299–324 (1984). https://doi.org/10.1016/0734-743X(84)90020-4.
[18] Rusinek A, Rodriguez-Martinez J A, Arias A, et al. Influence of conical projectile diameter on perpendicular impact of thin steel plate [J]. Engineering Fracture Mechanics, 2008, 75(10): 2946-2967. https://doi.org/10.1016/j.engfracmech.2008.01.011
[19] Iqbal M A, Diwakar A, Rajput A, et al. Influence of projectile shape and incidence angle on the ballistic limit and failure mechanism of thick steel plates[J]. Theoretical and Applied Fracture Mechanics, 2012, 62: 40-53. https://doi.org/10.1016/j.tafmec.2013.01.005
[20] Woodward RL, De Morton ME. Penetration of targets by flat-ended pro- jectiles. Int J Mech Sci 1976;18(3):119 – 27. https://doi.org/10.1016/0020-7403(76)90061-8
[21] Woodward RL. The penetration of metal targets by conical projectiles. Int J Mech Sci 1978;20(6):349 – 59. https://doi.org/10.1016/0020-7403(78)90038-3
[22] Woodward RL, Cimpoeru SJ. A study of the perforation of aluminium lami- nate targets. Int J Impact Eng 1998;21(3):117 – 31. https://doi.org/10.1016/S0734-743X(97)00034-1
[23] Chen X, Gao Y, He L. Analysis on the perforation of ductile metallic plates by APM2 bullets. Int J Prot Struct 2013;4(1):65 – 78. https://doi.org/10.4028/www.scientific.net/KEM.535-536.68
[24] Chen X, Li Q, Fan S. Oblique perforation of thick metallic plates by rigid projectiles. Acta Mech Sin 2006;22:367 – 76. https://doi.org/10.1007/s10409-006-0015-8
[25] Chen XW, Li W, Song C. Oblique penetration/perforation of metallic plates by rigid projectiles with slender bodies and sharp noses. Baozha Yu Chongji/Expolos Shock Waves 2005;25(5):393 – 9. https://doi.org/10.11883/1001-1455(2005)05-0393-07
[26] Jiao WJ, Chen XW. Influence of the mushroomed projectile's head geometry on long-rod penetration. Int J Impact Eng 2021;148:103769. https://doi.org/10.1016/j.ijimpeng.2020.103769
[27] Chen XW, Li QM. Shear plugging and perforation of ductile circular plates struck

by a blunt projectile. Int J Impact Eng 2003;28(5):513–36. https://doi.org/10.1016/S0734-743X(02)00077-5

[28] Sundaram S K, AG B, B A. Influence of target dynamics and number of impacts on ballistic performance of 6061-T6 and 7075-T6 aluminum alloy targets[J]. Mechanics Based Design of Structures and Machines, 2022, 50(3): 993-1011. https://doi.org/10.1080/15397734.2020.1738245

[29] Yiding Wu, Wencheng Lu, Minghui Ma, Yilei Yu, Xinyi Sun, Guangfa Gao, Analytical model of the perforation process of spherical-nosed projectiles impacting finite-thickness metal plates, Defence Technology, 54:134-150 https://doi.org/10.1016/j.dt.2025.07.018

[30] Yiding Wu, Wencheng Lu, Xinyu Sun, Shuangqi Li, Bingzhuo Hu, Guangfa Gao, Penetration behavior and energy-partition mechanisms of a 12.7 mm armor-piercing incendiary projectile into semi-infinite steel targets, International Journal of Impact Engineering, 2026，212:0734-743X https://doi.org/10.1016/j.ijimpeng.2026.105662

[31] Lei Jinwei, Song Jiaqi. Study on Penetration Law of Tungsten Alloy Frag ments into Q235 Steel Targets[J]. Packaging Engineering, 2024, 45(23). A2 75A3E1994F4373837292F4E9529C49. https://doi.org/10.19554/j.cnki.1001-3563.2024.23.032

[32] Xia Jingwen, Chen Zhigang, Gu Minhui, et al. Numerical Simulation Study on Penetration of 2024 Aluminum Target by Tungsten Alloy Fragments[J]. Journal of Vibration and Shock, 2023, 42(15). E27A3865C52441CF95688C 716894A21C. https://doi.org/10.13465/j.cnki.jvs.2023.15.019

[33] Jia Guilong, Zhang Hang, Rao Qingdong, et al. Air Cushion Suspension Heat Treatment Process of 2A12 Aluminum Alloy Skin Plate for Aerospace[J]. Heat Treatment of Metals,2025,50(8):127-136. https://doi.org/10.13251/j.issn.0254-6051.2025.08.021.

[34] Hu Jing, An Jingdan. Research on Anti-Impact Characteristics of Single-Layer 2A12 Aluminum Alloy Plate Subjected to Flat-Headed Projectiles[J]. Journal of Mechanical Strength,2022,44(01).0CE7057E57A24D97A847ED3EB19D14F1. https://doi.org/10.16579/j.issn.1001.9669.2022.01.009

[35] Hao Peng, Qing Guanghui, Li Jianfeng, Deng Yunfei, Wei Gang. Research on Anti-Impact Performance of Thin 2A12 Aluminum Alloy Plates against Ogival-Nosed Projectiles[J]. Journal of Vibration and Shock,2016,35(17).93EE53B1B3B3406F9D3589884FEFAE7C. https://doi.org/10.13465/j.cnki.jvs.2016.17.004

[36] Wu Y , Lu W , Yu Y ,et al.Penetration Mechanics of Finite -Thickness Aluminum Alloy Plates: A Review of High-Strain -Rate Behavior and Predictive[J].Mechanics of solids, 2025(4): 60. https://doi.org/10.1134/S0025654425601624

[37] Li Jinfu, Zhi Xiaoqi, Fan Xinghua. Study on the Penetration Characteristics of Tungsten Spheres and Hexagonal Tungsten Rod Fragments into Q235 Laminated Targets [J] Journal of Artillery Firing and Control, 2021, 42(02): 28-33+39. https://doi.org/10.15892/j.cnki.djzdxb.2020.04.012

[38] Wang Xiaobing, Wang Weibao, Hu Hao, et al. Simulation analysis of prefabricated tungsten fragment armor piercing [J]. China Manufacturing Informationization, 2008, 37(24): 71-72+78. https://doi.org/CNKI:SUN:JXZZ.0.2008-24-033

[39] Buyuk M, Kurtaran H, Marzougui D, et al. Automated design of threats and shields under hypervelocity impacts by using successive optimization methodology[J]. International Journal of Impact Engineering, 2008, 35(12): 1449-1458. https://doi.org/10.1016/j.ijimpeng.2008.07.057

[40] Hao, B., Dong, Z., Xu, C. et al. Influence of Fragment Morphology on the Penetration Behavior of Curved Thin-Shell Structures. Mech. Solids 61, 6086–6100(2026). https://doi.org/10.1134/S0025654426600273